Widespread Remodeling of Synaptic Protein Interaction Networks Following Homeostatic Plasticity in Cortical Neurons Requires Homer1 and Shank3

Authors: Whitney E. Heavner[1], Haley E. Speed[1], Jonathan D. Lautz[1], Edward P. Gniffke[1], Karen B. Immendorf[1], John P. Welsh[1,2,3,4], and Stephen E.P. Smith[1,2,4*]

Affiliations: 1. Center for Integrative Brain Research, Seattle Children's Research Institute, Seattle, WA. 2. Department of Pediatrics, University of Washington School of Medicine, Seattle, WA. 3. University of Washington Autism Center, Seattle, WA. 4. Graduate Program in Neuroscience, University of Washington, Seattle, WA.
*Correspondence: seps@uw.edu

Keywords

Autism, Homeostatic plasticity, Synaptic Scaling, Signal transduction, Synapse, Neural activity, Protein interaction network

Summary

Neurons maintain constant levels of excitability using homeostatic scaling, which adjusts relative synaptic strength in response to large changes in overall activity. While previous studies have catalogued the transcriptomic and proteomic changes associated with scaling, the resulting alterations in synaptic protein interaction networks (PINs) are less well understood. Here, we monitor a glutamatergic synapse PIN composed of 380 binary interactions among 21 protein members to identify protein complexes altered by synaptic scaling. In cultured cortical neurons, we observe widespread bidirectional PIN alterations with up- versus downscaling. In the barrel cortex, the PIN response to 48 hours of sensory deprivation exhibits characteristics of both upscaling and downscaling, consistent with emerging models of excitatory/inhibitory balance in cortical plasticity. Mice lacking *Homer1* or *Shank3B* do not undergo normal PIN rearrangements, suggesting that these Autism Spectrum Disorder (ASD)-linked proteins serve as structural hubs for synaptic homeostasis. Our approach demonstrates how previously identified RNA and protein-level changes induced during homeostatic scaling translate into functional PIN alterations.

Introduction

Neurons maintain constant relative cell-wide synaptic strengths, despite varying network activity, through a non-Hebbian form of neural plasticity called homeostatic synaptic scaling (Turrigiano et al., 1998). At the molecular level, homeostatic scaling adjusts the number of postsynaptic glutamate receptors up or down to compensate for prolonged decreased or increased synaptic activity, without compromising the distributed information content of each synapse (Fong et al., 2015; Goel and Lee, 2007; Hu et al., 2010; O'Brien et al., 1998; Pozo and Goda, 2010; Turrigiano, 2012). In addition to, or in cooperation with, other homeostatic mechanisms, such as intrinsic homeostatic plasticity (Desai et al., 1999a) and sliding-scale plasticity (Bienenstock et al., 1982), synaptic scaling *in vivo* restores the activity of a neuron to an initial set point after prolonged sensory deprivation (Hengen et al., 2013, 2016) or prolonged activation (Goold and Nicoll, 2010) (reviewed in (Turrigiano, 2011)). Homeostatic plasticity is thought to be crucial for preventing synaptic saturation, thus allowing for new memory formation, and may be disrupted in several neurological disorders, including Alzheimer's

disease (Styr and Slutsky, 2018) and ASD (Antoine et al., 2019; Bülow et al., 2019; Jewett et al., 2018; Tatavarty et al., 2018).

Prior studies have catalogued extensive molecular alterations associated with homeostatic scaling. At the most basic level, upscaling is mediated by insertion of GluR2-contianing AMPA receptors and alterations in AMPA receptor co-association with synaptic scaffolds (Gainey et al., 2009). Additional critical molecular pathways have been evaluated using single candidate-based approaches. For example, fluctuations in intracellular Ca^{2+} levels lead to CaMKIV activation, which drives changes in gene expression (Ibata et al., 2008) and downstream synaptic accumulation of trafficking proteins, such as GRIP1 (Gainey et al., 2015). Activity blockade de-represses retinoic acid synthesis, leading to increased local translation and synaptic insertion of AMPA receptors (Aoto et al., 2008). The immediate early gene *Homer1a*, its binding to the metabotropic glutamate receptor mGluR5 (Diering et al., 2017; Hu et al., 2010), the chromatin reader *L3mbtl1*, and the scaffolding protein/transcription factor *Ctnnb1* (Mao et al., 2018) all play important roles. In addition, widespread changes in protein ubiquitination have been documented during scaling (Ehlers, 2003), and omics-scale studies have catalogued extensive alterations to the transriptome (Ibata et al., 2008; Mao et al., 2018; Schaukowitch et al., 2017; Steinmetz et al., 2016) and proteome (Schanzenbächer et al., 2016, 2018). These changes in transcript and protein abundance are often bidirectional, or opposite, for upscaling versus downscaling. Taken together, these studies highlight a complex molecular process through which changes in synaptic activity lead to compensatory changes in synaptic excitability.

Just as mRNA levels do not predict protein expression in complex systems (Gygi et al., 1999; Jovanovic et al., 2015), protein levels alone do not determine physiological outcomes. The relationships between newly synthesized or degraded molecules and the existing protein complexes in the cell determine the physiological effects of altered protein turnover. In addition to absolute protein abundance, protein complex composition is further influenced by post-translational modifications and the presence or absence of functional binding partners. In fact, the combinatorial complexity of the protein interactome, as well as its incomplete characterization (Cafarelli et al., 2017), make predicting the physiological effect of altered protein abundance exceedingly difficult. Here, by focusing on the macromolecular protein complexes that control the localization of glutamate receptors at the postsynapse, we bridge

the gap between these well-characterized protein abundance changes and the electrophysiological effects that occur during homeostatic scaling. Using an emerging proteomic technique, Quantitative Multiplex co-Immunoprecipitation (QMI), we characterize changes to a synaptic PIN consisting of 21 unique synaptic proteins (380 binary interactions) following upscaling and downscaling and demonstrate how altered protein production and degradation result in widespread, coordinated changes to the functional PINs that mediate synaptic excitability. Moreover, using sensory deprivation in two different mouse models of ASD, we demonstrate that the synaptic scaffolding proteins Homer1 and Shank3 are required for PIN rearrangements characteristic of homeostatic plasticity *in vivo*.

Results

Upscaling and downscaling induce distinct changes in protein interaction networks

We cultured dissociated cortical neurons from postnatal day (P) 0 wild-type mice for 15-19 days, then treated each culture for 48 hours with tetrodotoxin (TTX, 2μM) to induce upscaling, bicuculine (BIC, 40μM) to induce downscaling, or dimethylsulfoxide (DMSO, 0.4%) as a vehicle control. We confirmed upscaling and downscaling using surface expression of GluR1 (Diering et al., 2014), which was significantly elevated after TTX treatment and reduced after BIC treatment (fold-change=2.32 and 0.256, *P*-value=0.04 and 0.01, respectively) (**Fig. 1A**). Previous studies have reported widespread changes in the levels of synaptic proteins after 2 to 72 hours of upscaling or downscaling *in vitro* (Ehlers, 2003; Schanzenbächer et al., 2016, 2018), so we quantified total protein levels of several synaptic proteins by western blot after 24 and 48 hours of scaling (**Fig. 1B, C**). After 24 hours of downscaling, we observed a significant decrease in PSD95 (*P*=0.03), Fyn (*P*=0.005), and the glutamate receptors GluR1 (*P*=0.003) and mGluR5 (*P*=0.01), consistent with previous reports (Ehlers, 2003; Sun and Turrigiano, 2011) (Schanzenbächer et al., 2016). By contrast, after 24 hours of upscaling, only mGluR5 changed significantly (*P*=0.005), and was increased, opposite downscaling. Similarly, GluR1 tended to increase but was not statistically significant (*P*=0.1). After 48 hours of upscaling, however, GluR1 was significantly increased (*P*=0.03), while mGluR5 levels appeared to have normalized, and Homer1 was significantly reduced (*P*=0.03). By contrast, mGluR5, PSD95, and Fyn remained reduced after 48 hours of downscaling (*P*=0.009, 0.007, and 0.04, respectively), while

GluR1 levels appeared to have normalized, and Homer1 was slightly but significantly reduced (P=0.05).

Prolonged changes in neural activity have been shown to affect the MEK-ERK pathway, leading to bidirectional changes in ERK1/2 phosphorylation upstream of changes to activity-dependent mRNA and protein production (Bateup et al., 2013). We measured the relative levels of phosphorylated (p-) ERK1/2 after 24 and 48 hours of TTX, BIC, or DMSO **(Fig. 1D)** and found that TTX caused a significant decrease in the ratio of p-ERK1/2 to total ERK1/2 compared with DMSO after 24 hours (P=0.004), which remained significantly decreased after 48 hours (P=0.02). Conversely, BIC increased the ratio of p-ERK1/2 to total ERK1/2 after 24 hours (P=0.02), which normalized after 48 hours, potentially as a result of negative feedback onto p-ERK1/2 through changes to surface glutamate receptors (Bateup et al., 2013; Chowdhury et al., 2006). Together with the above data, these results demonstrate that prolonged activity perturbation alters surface GluR1, synaptic protein abundance, and ERK1/2 activation consistent with prevailing views of homeostatic scaling.

The quantitative multiplex immunoprecipitation (QMI) panel described in this report contains 21 validated synapse-associated proteins- receptors, scaffolds, and downstream signaling molecules **(Table 1)** and measures 380 binary PiSCES for each experiment (Lautz et al., 2018, 2019). QMI takes advantage of fluorophore-embedded microspheres ("beads") to immunoprecipitate multiple protein targets from a single sample simultaneously (Lautz et al., 2018; Smith et al., 2016). Biotinyated probe antibodies detect co-associated proteins, and, following streptavidin-PE secondary labeling, the median fluorescence intensity (MFI) of each IP-probe combination is measured on a flow cytometer and averaged across technical replicates (see methods) **(Fig. 1E)**. We refer to multiprotein complexes detected by QMI as "Proteins in Shared Complexes detected by surface Epitopes" (PiSCES), to highlight the fact that the measured interactions are not necessarily direct. Using this QMI panel, we evaluated changes in synaptic protein complexes after 48 hours of upscaling or downscaling.

Network-level differences in PiSCES between TTX, BIC, and DMSO-treated cells (N=4 biological replicates) were evaluated using hierarchical clustering and principal component analysis (PCA). The three treatment conditions clustered into three discrete groups, and PCA showed separation of the three conditions along principal component (PC) 1 (**Fig. 1F**). These

results demonstrate that there is more similarity within a treatment group than between groups and imply that prolonged increased or decreased activity causes distinct network-level changes in synaptic PINs in addition to changes in protein synthesis and degradation.

Upscaling and downscaling induce bidirectional and unidirectional changes *in vitro*

To better understand the PIN rearrangements that occur during homeostatic scaling, we identified a set of high-confidence PiSCES that changed individually after drug treatment *and* belonged to a module of interactions that correlated with the drug treatment using a combination of two statistical tests: 1) adaptive nonparametric analysis with an empirical alpha cutoff (ANC) and 2) weighted correlation network analysis (CNA) (Langfelder and Horvath, 2008), as described in (Smith et al., 2016). ANC, which identifies PiSCES with different bead distributions between conditions, identified 27 PiSCES that changed significantly with TTX treatment and 16 that changed with BIC treatment (multiple-comparison-corrected *P*-value<0.05); 8 PiSCES were significant in both conditions **(Table S1).** CNA identified five modules of PiSCES that changed in a correlated manner, presumably as part of a PIN **(Fig. 2A,B)**. The CNA module that showed the most significant correlation with a treatment was the "turquoise" module, which was positively correlated with TTX (P=6x10^{-5}) and negatively correlated with BIC (P=0.01), suggesting bidirectional effects on module members. Moreover, the turquoise module was most strongly correlated with treatment when TTX and BIC were coded as "opposites" (P=2x10^{-5}) **(Fig. 2B)**. Conversely, one module, the "brown" module, was correlated with treatment (P=0.009), regardless of condition, indicating unidirectional changes of module members. Importantly, neither module correlated with experiment number, ruling out batch effects.

To visualize the behaviors of individual PiSCES in different modules and increase confidence in ANC-signficant true positives, we took a reductionist approach and evaluated by heatmap PiSCES that were ANC-significant in either the BIC or TTX condition and correlated with a given module (P<0.05, |module membership|>0.7) (**Fig. 2C**). For the turquoise module, unsupervised clustering clearly separated TTX, BIC and DMSO conditions, and the row-normalized values showed that BIC and TTX had opposite effects on PiSCES when compared with DMSO, a veritable intermediate. The clustering pattern of the brown module indicated

reduced MFIs in the TTX and BIC conditions compared with DMSO, but one of the TTX replicates clustered with DMSO and vice-versa (**Fig. 2D**).

PiSCES changes in each condition were visualized by nested network diagrams (**Fig. 2C,D**). The turquoise module contained PiSCES that reflected shuttling of AMPA and mGluR receptors in and out of the membrane (**Fig. 2C**). GluR2_GluR1 and GluR2_PSD95 both increased with TTX and decreased with BIC, while the amount of mGluR5 co-associated with its major scaffolding protein Homer1 (and Homer1a) followed a similar pattern. These data are consistent with upregulation of mGluR and AMPAR signaling during upscaling and downregulation during downscaling (Aoto et al., 2008; Gainey et al., 2009; Hu et al., 2010) . In fact, Homer1_mGluR5 was the single largest $\log_2$(fold change) we detected, and it has been shown that mGluR interaction with Homer1a, which affects its axonal and dendritic targeting and interaction with the Homer/Shank scaffold (Ango et al., 2000; Tu et al., 1999), is critical for the expression of homeostatic plasticity (Diering et al., 2017). Scaffolding protein rearrangements were also prevalent in the turquoise module: PSD95_SAP97, SAP97_ SAPAP, Shank1_ SAPAP, and Homer1_SAPAP were increased with TTX/decreased with BIC, reflecting rearrangement of Shank and DLG family scaffolds. These interactions have been suggested to play a vital role in scaling, during which phosphorylation of SAPAP proteins by CaMKII regulates the turnover of AMPARs (Rasmussen et al., 2017). Conversely, PiSCES involving Shank1 and Homer1 with panShank decreased with TTX and increased with BIC.

The brown module contained PiSCES that decreased after both upscaling and downscaling, which could suggest a PIN that dissociates after prolonged changes in activity, regardless of whether activity is increased or decreased. This module included several PiSCES containing the kinse Fyn, which phosphorylates both NMDAR2B and mGluR1 (Jin et al., 2017; Nakazawa et al., 2001; Yang and Leonard, 2001)), and mGluR5_Fyn co-association was significantly reduced following TTX treatment (**Fig. 2D**). The imperfect clustering of TTX1 within the brown module, however, reduced our confidence that the PiSCES within this module were true positives. We therefore asked how reproducible PiSCES measurements were across multiple experiments. We performed two additional sets of experiments for a total of three sets of TTX, BIC, or DMSO applied for 48 hours (N=4,4,5 per set) (**Fig. 3**). For each set, we performed ANC∩CNA analysis as described above, requiring that “significant PiSCES” pass both CNA and ANC criteria. For TTX, only five PiSCES met the stringent ANC∩CNA criteria for all three

sets (mGluR5_mGluR5, mGluR5_Homer1a, Homer1_mGluR5, Homer1_SAPAP, and Homer1_panShank), and only four for BIC (Homer1_panShank, mGluR5_Homer1a, SAP97_PSD95, and PSD95_PSD95). Moreover, many PiSCES were significant in only one set (**Fig. 3A**). Conversely, when we compared sets that were run in parallel (on the same QMI plates), we found high concordance for the same condition (24 shared significant PiSCES, R^2=0.97, N=4 per set), and low concordance for different conditions (R^2=0.17) **(Fig. S1A,B)**.

To differentiate between overly stringent statistics (true positives are missed) and a noisy analytical platform (false positives are identified), we ran CNA on the full set of 39 samples across the three sets (**Fig. 3B**). A turquoise module that was positively correlated with TTX (P=5x10^{12}) and negatively correlated with BIC (P=7x10^{-7}) was again identified. This module contained 28 of the 47 (60%) PiSCES that were significant in at least one of the three sets, 26 of which were significant module members (P<0.05). When these PiSCES were plotted as a heatmap and ordered using unsupervised clustering, samples clustered by treatment type, and a clear pattern emerged in which PiSCES changed bidirectionally between TTX and BIC treatment, while DMSO served as an intermediate (**Fig 3B,C**). Critically, PiSCES in the turquoise module that were significant in only one of the three sets (such as GluR2_PSD95) tended to follow the same trend in all sets but did not reach the stringent ANC∩CNA criteria every time (**Fig. 3D**). These data suggest that each experimental set identified a subset of the total PiSCES that change during homeostatic scaling, and were consistent with reproducibility rates reported for mass spectrometry (Gonzalez-Lozano et al., 2020; Tabb et al., 2010).

Several modules only marginally correlated with treatment ("blue," "brown," and "yellow"), and each contained a few additional ANC-significant PiSCES (**Fig. 3B**), but samples did not segregate by treatment within these modules**,** so these PiSCES cannot be ruled out as experimental or biological noise. Moreover, most of the additional significant PiSCES were in the brown module and co-varied with each other (appeared together, right of center of the cluster dendrogram in **Fig. S2)**. We therefore hypothesize that they represent true, biologically-relevant modules of interacting proteins, here consisting primarily of Shank1, SynGAP, and Fyn, that co-vary in cultured cells, but are unrelated to TTX/BIC treatment. Taken together, these results identify a high-confidence set of multiprotein complexes that rearrange bidirectionally during 48 hours of homeostatic upscaling vs. downscaling, as well as a 'biological noise' module.

Protein interaction changes broadly stabilize by 12 hours of upscaling or downscaling

Different sets of proteins are newly synthesized after prolonged activity perturbations for a time period lasting at least 2-24 hours (Schanzenbächer et al., 2016, 2018). We therefore asked whether different PiSCES changed at different timepoints over a 48-hour period of upscaling or downscaling. We performed QMI after 12 hours and 24 hours of TTX and BIC treatment and compared PiSCES changes between all three time points (using 48 hours, set 2 from above). Hierarchical clustering of all interactions (MFI>100) separated TTX, BIC, and DMSO conditions into discrete groups (**Fig. 4A**). Approximately unbiased (AU) *P*-values, determined by multiscale bootstrap resampling, identified three major clusters correlated with treatment: **1)** all TTX samples formed one cluster, **2)** BIC 48 hours formed an independent cluster, and **3)** BIC 12 hours and BIC 24 hours clustered with DMSO. Similarly, PCA showed that all three TTX groups separated from DMSO control groups along PC1 (**Fig. 4B**). By contrast, the BIC 12 hour group overlapped with the DMSO groups, but the BIC 24 and 48 hour groups separated from DMSO along PC1 in the opposite direction of TTX.

We next used CNA as described above to identify high-confidence PiSCES that changed together in response to treatment. We identified one major bidirectional module similar to the two turquoise modules described above (**Fig. 4C**). When we asked if any timepoint alone was better correlated with this module than TTX or BIC treatment as a group, we saw that the 12 hour timepoint showed no correlation, the 24 hour timepoint showed some correlation but was only significant for TTX, and the 48 hour timepoint showed strong correlation for both TTX and BIC, although neither was as correlated as TTX or BIC coded independent of time. Collectively, these data demonstrate that TTX and BIC induce PiSCES changes that are consistently bidirectional over 48 hours.

Three additional modules (“black,” “green,” and “yellow”) were weakly correlated with individual timepoints (**Fig. 4C**) but contained few if any ANC-significant PiSCES and/or were dominated by a single antibody, suggesting a technical artifact. The brown module contained five ANC-significant PiSCES but did not correlate with treatment or timepoint and contained many of the same PiSCES in the noise module described in the N-of-12 analysis (containing

Shank1, Homer1, and SynGAP interactions). Collectively, the ANC-significant PiSCES in these additional modules were considered to be the result of biological or technical noise.

To explore the individual PiSCES that contributed to the bidirectional turquoise module, we merged ANC hits at each timepoint with turquoise module members (**Fig. 4D,E**). At 12 hours, 6 PiSCES were identified for TTX, and 7 for BIC, all of which were significant in at least one other timepoint. For TTX, all of these PiSCES were consistently elevated, with the exception of SynGAP_SynGAP. GluR2_GluR1, which reflects AMPA receptor insertion, and several Homer1-containing interactions, including Homer1_mGluR5, were elevated at 12 hours and remained elevated throughout the timecourse (**Fig. 4E**). Collectively, these PiSCES demonstrate a rapid remodeling of the Homer scaffold, which adjusts mGluR tone, as well as rapid AMPAR insertion during upscaling. Moreover, the Homer1-containing PiSCES that were significantly increased during upscaling were decreased during downscaling, and SAP97_PSD95 was significantly decreased throughout the downscaling timecourse, reflecting synapse weakening from 12 hours onward (Cai et al., 2006). Conversely, Shank- and SynGAP-containing PiSCES were increased during downscaling at 12 hours.

By 24 hours, TTX and BIC produced 9 and 11 altered PiSCES, respectively. By 48 hours, 9 additional PiSCES were significant for TTX, and two additional PiSCES were significant for BIC. It is interesting to note that Fyn interaction with the NMDA receptors 2A and 2B appeared decreased during upscaling and increased during downscaling at 48 hours, reflecting Fyn modulation of NMDAR function in response to prolonged activity perturbation (Trepanier et al., 2012). Collectively, these data reveal that most PiSCES changes characteristic of homeostatic scaling occur during the first 12 hours of prolonged activity perturbation, but some changes do not reach statistical significance until 24 or 48 hours.

Sensory deprivation induces a homeostatic response in the barrel cortex

We have identified a set of high-confidence PiSCES that correlate with synaptic scaling over 12-48 hours *in vitro*. We next asked how homeostatic plasticity *in vivo* compares with synaptic scaling *in vitro*: do the same sets of PiSCES that change during synaptic scaling also change during prolonged activity manipulation *in vivo*?

Extreme alteration of activity using sensory deprivation and/or stimulation has been shown to induce homeostatic plasticity *in vivo* (Bridi et al., 2018; Desai et al., 2002; Glazewski et al., 2017; Goel and Lee, 2007; Hengen et al., 2013; Knogler et al., 2010; Kotak et al., 2005). Sensory deprivation of the visual cortex, for example, reduces cortical inhibition, which increases spontaneous activity and lowers the threshold for LTP (Benevento et al., 1992; Bridi et al., 2018; Kirkwood et al., 1996; Kuhlman et al., 2013). Similarly, whisker trimming, an established model for sensory deprivation of somatosensory (barrel) cortex (Gainey et al., 2016, 2018; Gray et al., 2006), has been shown to increase the ratio of excitation to inhibition (E/I): while both excitation and inhibition decrease after whisker trimming, inhibition decreases more (Gainey et al., 2018; Li et al., 2014). Given the evidence that sensory deprivation alters both excitation and inhibition, we asked whether whisker trimming induces an upscaling or downscaling-like homeostatic PIN response.

To test whether we could induce a homeostatic response *in vivo*, we trimmed the whiskers on one side of an adult mouse (age 7-9 weeks) (**Fig. 5A**). After 48 hours, we investigated the functional consequences of whisker trimming by measuring miniature excitatory postsynaptic potentials (mEPSCs) from Layer II/III (L2/3) pyramidal neurons of barrel cortex. The hemisphere ipsilateral to the whisker trim (control side) exhibited a mean amplitude and frequency similar to other reports on WT L2/3 pyramidal cells (**Fig. 5B-D**; frequency: 1.87 ± 0.42 Hz; Amplitude: -8.22 ± 2.83 pA) (Michaelson et al., 2018). Neurons from the contralateral hemisphere (trimmed side), however, demonstrated a 2-fold increase in mean frequency compared with the ipsilateral hemisphere (**Fig. 5B,D**; 3.85 ± 0.59 Hz; Student's t-test, $P = 0.0035$) with no change in mean mEPSC amplitude (**Fig. 5C,D**; -6.19 ± 1.18 pA). Cumulative analysis of inter-event intervals revealed a global trend toward decreased time between events onto neurons from the contralateral hemisphere compared with those from the ipsilateral hemisphere (**Fig. 5E**, Kolmogorov-Smirnov, $P = 0.0242$), consistent with an increase in mean mEPSC frequency. Moreover, the cumulative probability of mEPSC amplitude was skewed, revealing a trend toward smaller events that was not reflected in the mean amplitude (**Fig. 5F vs. Fig. 5C**), and there was no difference in spine density between ipsilateral and contralateral hemispheres (**Fig. 5G;** 17.25 +/-2.44 vs. 17.13 +/- 1.86 spines/10 microns). Taken together, our data confirm that whisker deprivation induced a homeostatic response in the contralateral hemisphere 48 hours after trimming, as previously reported (Gainey et al., 2016, 2018; Knott et al., 2002; Li et al., 2014).

To identify differences in PiSCES between trimmed and control sides, we micro-dissected the barrel cortex from five coronal slices and separated the hemispheres into contralateral ("trimmed") and ipsilateral ("control") sides, homogenized the tissue in lysis buffer, and ran QMI (**Fig. 5A**). PCA and hierarchical clustering of all interactions (MFI>100) showed separation of control and trimmed sides (**Fig. 5H,I**). The intersection of ANC-significant PiSCES with PiSCES that were in a CNA module significantly associated with whisker trimming yielded 14 PiSCES. A heatmap of the MFIs of all 14 showed consistent differences between control and trimmed sides (**Fig. 5J**). Seven (50%) of these PiSCES were also members of at least one bidirectional CNA module identified in the *in vitro* timecourse experiments above, suggesting that whisker trimming induces PiSCES changes *in vivo* that are distinct from changes observed *in vitro*.

To distinguish between true and false positives, we performed two more sets of whisker trimming (N=6 for set 1, 4 for sets 2,3) for a total of 14 control and 14 trimmed samples (**Fig. S3**). Hierarchical clustering completely separated control and trimmed samples and identified two significant clusters with an AU *P* value>0.9 (11 samples in each cluster) (**Fig. S3A**). To idenfity modules of PiSCES significantly correlated with whisker trimming, we used CNA of all 28 samples together and intersected PiSCES in these modules with ANC-significant PiSCES from any single set **(Fig. S3B).** CNA of all samples identified two modules ("turquoise" and "green") that were significantly correlated with whisker trimming. The turquoise and green modules contained 14 and 8 ANC-significant PiSCES, respectively, which showed clear segregation of conditions when plotted by heatmap **(Fig. S3C)**. The "blue" and "yellow" modules contained three and two additional ANC-significant PiSCES, respectively, but these did not show clear segregation by condition. Finally, the "brown" module contained 3 ANC-significant PiSCES and was marginally correlated with cortical hemisphere; however, only Homer1_panShank showed clear segregation by hemisphere when plotted by heatmap (higher MFI in the right hemisphere) (**Fig. S3C**). Together, the 22 ANC-significant PiSCES in the turquoise and green modules (the only modules in which PiSCES segregated by trimming) represent high-confidence PiSCES that change in response to whisker trimming.

We next asked how similar these *in vivo* changes were with *in vitro* synaptic scaling. We first compared the direction of the change of each of the 22 high-confidence PiSCES *in vivo* with the behavior of these PiSCES *in vitro* (**Fig. 6A,B**). Naïve hierachcial clustering on these 22

PiSCES separated control and trimmed samples and revealed that most PiSCES increased after trimming (**Fig. 6A**). Of the 22 high-confidence PiSCES that changed *in vivo*, 10 (45%) were significant at some point during the *in vitro* timecourse described above. The direction of the change *in vivo* was consistent with TTX treatment 6 out of 10 times and consistent with BIC treatment 4 out of 10 times (**Fig. 6B**), suggesting that sensory deprivation induces a homeostatic response distinct from homeostatic synaptic scaling, at least when limited to the 22 high-confidence PiSCES that changed *in vivo*.

Limiting the comparison between *in vitro* and *in vivo* homeostatic plasticity to these 22 PiSCES, however, may ignore subtle differences between all high-confidence PiSCES from all *in vivo* and *in vitro* experiments. To determine if changes in all high-confidence PiSCES after whisker trimming were more similar to upscaling or downscaling, we used t-distributed Stochastic Neighbor Embedding (tSNE) of mean $\log_2$(fold change) values (Maaten and Hinton, 2008) and visualized clustering in 2 dimensions (**Fig. 6C**). For tSNE, we included seven TTX sets (N=4 biological replicates per set) over three time points, seven BIC sets over three time points, and 3 sets of whisker trimming. To control for *in vitro* versus *in vivo* bias, we included a set of *in vivo* experiments that compared the effects of treatment with the strong GABA(A) receptor agonist THIP (10mg/kg IP) with the effects of PBS-treatment on the barrel cortex (48 hours) (Bridi et al., 2018; Drasbek and Jensen, 2006) . We also included one whisker trim+THIP vs. non-trimmed+THIP set and one *in vitro* THIP (20μM) set for a total of 20 sets for input into tSNE.

We first used PCA to determine how THIP treatment affected PiSCES *in vitro* and *in vivo* **(Fig. S4)**. *In vitro* THIP-treated samples segregated with TTX-treated samples along PC1 and with BIC-treated samples along PC2, but did not overlap with either. Similarly, THIP injection *in vivo* segregated with whisker trimming along PC1 and with THIP+whisker trimming along PC2, suggesting that THIP treatment has a unique effect compared with TTX/BIC *in vitro* and with whisker trimming *in vivo,* and therefore serves as a useful *in vitro* vs. *in vivo* control. tSNE of mean $\log_2$(fold changes) of all high confidence PiSCES across all 20 sets revealed that all TTX samples formed one isolated cluster, with the exception of one 24-hour set. The BIC sets formed two clusters, the larger of which contained both the *in vitro* and *in vivo* THIP sets. Critically, all four whisker trimming sets formed one independent cluster, further suggesting

that whisker trimming causes a homeostatic response distinct from synaptic upscaling and downscaling.

To determine which PiSCES most contributed to the differences between whisker trimming, TTX treatment, and BIC treatment, we performed pairwise Wilcoxon rank-sum tests of all PiSCES. PiSCES with the most significant pairwise differences are shown in **Table S2**. The most significant differences (lowest *P* values) were between the TTX and BIC groups. Interestingly, several PiSCES were significantly different between whisker trimming and both *in vitro* groups, including Homer1_mGluR5, mGlur5_Fyn, and Ube3a_Ube3a. Box-and-whisker plots of mean $\log_2$(fold changes) of several of the most significantly different PiSCES revealed that some PiSCES, including Ube3a_Shank3 and CaMKII_Homer1a, appeared to change only with TTX and/or BIC treatment (**Fig. 6D**). Some PiSCES *in vivo* behaved similarly to TTX, including mGluR5_panHomer, mGluR5_Homer1a, Homer1_SAPAP, and SAP97_PSD95, while some behaved similarly to BIC, including Homer1_mGlur5, PSD95_PSD95, and NL3_PIKE. Moreover, some PiSCES appeared to change only with whisker trimming, including mGluR5_Fyn, Fyn_Fyn, and Ube3a_Fyn (**Fig. 6D**), suggesting that prolonged sensory deprivation induces PiSCES changes that are specific to *in vivo* homeostatic plasticity.

Homer1 and Shank3 are synaptic hubs for homeostatic plasticity

We have demonstrated that many interactions involving the synaptic scaffolding protein Homer1 and its short dominant-negative isoform Homer1a are bidirectional between upscaling and downscaling *in vitro*. Moreover, Homer1a is required for downscaling during sleep (Diering et al., 2017), and four PiSCES involving Homer1 and/or Homer1a changed significantly after whisker trimming. We therefore asked whether Homer1 is required for synaptic PIN rearrangements after whisker trimming. We trimmed the whiskers on one side of mice lacking exon 2 of *Homer1* and therefore lacking expression of both short and long isoforms of *Homer1* (Yuan et al., 2003). We then measured PiSCES by QMI. PCA of all PiSCES (MFI>100) in all four conditions (WT trimmed, WT control, KO trimmed, KO control) revealed that WT and KO samples, regardless of trimming, separated along PC1, while WT trimmed and control samples separated along PC3 (**Fig. 7A**); however, KO trimmed and control samples showed no clear separation.

To visualize interactions that were significantly different between trimmed and control sides in both WT and KO barrel cortex, we plotted by heatmap all PiSCES that were significantly altered according to at least one of three pairwise comparisons (WT control vs. WT trimmed, KO control vs. KO trimmed, and WT control vs. KO control) (**Fig. 7C,D**). Three PiSCES that were elevated after whisker trimming, including Shank1_NMDAR2B, Shank1_Fyn (**Fig. 7G**), and mGluR5_Fyn (**Fig. 7H**), were already elevated in the *Homer1* KO barrel cortex with or without whisker trimming. Conversely, Shank1_Homer1a (**Fig. 7I**), which increased after whisker trimming in WT mice, was decreased in the *Homer1* KO barrel cortex with or without whisker trimming. When the MFIs of PiSCES that changed significantly only after whisker trimming (**dashed box in Fig. 7C**) were plotted in separate heatmaps for WT and KO samples, a clear trend was observed: WT trimmed and control sides, but not KO trimmed and control sides, could be distinguished (**Fig. 7D**). Two PiSCES involving SynGAP (SynGAP_SynGAP and SynGAP_PSD95), however, increased after whisker trimming in both WT and KO barrel cortex. Together, these findings suggest that whisker trimming has little to no effect on PIN rearrangements in the sensory-deprived barrel cortex of mice lacking *Homer1*.

Homer1 may drive homeostasis through its interactions with other synaptic proteins in the network that responds to prolonged increases in network activity, including the Shank family of scaffolding proteins. Human *SHANK3* is disrupted in an ASD-associated syndrome called Phelan-McDermid Syndrome (Phelan and McDermid, 2012; Wilson et al., 2003) and has been suggested to play a role in homeostatic plasticity *in vitro* and firing rate recovery in the mouse visual cortex after visual deprivation (Tatavarty et al., 2018). To determine if *Shank3*, like *Homer1*, is required for PIN rearrangements observed after whisker trimming, we trimmed the whiskers on one side of *Shank3B* KO mice (Peça et al., 2011) and measured PiSCES by QMI. PCA of all PiSCES (MFI>100) of all four conditions revealed that WT and KO control samples separated along PC1 and PC2 but were not as distinct as the *Homer1* WT and KO groups (**Fig. 7B vs. 7A**). WT trimmed and control samples also separated along PC1 and PC2, while KO trimmed and control samples showed no clear separation and, moreover, overlapped substantially with the WT trimmed group (**Fig. 7B**).

We plotted all significantly altered PiSCES from the three pairwise comparisons described above by heatmap (**Fig. 7E,F**). Like PiSCES in the *Homer1* KO barrel cortex, many of the

PiSCES that were elevated after whisker trimming in WT controls were already elevated in the *Shank3B* KO barrel cortex without whisker trimming, including SAP97_PSD95 (**Fig. 7J**), PSD95_PSD95 (**Fig. 7K**), and NMDAR2A_NL3. Conversely, Homer1_Shank3 appeared to increase after whisker trimming in WT mice but was substantially decreased in the *Shank3* KO barrel cortex with and without whisker trimming. When the MFIs of PiSCES that changed significantly only after whisker trimming (**dashed box in Fig. 7E**) were plotted in separate heatmaps for WT and KO samples, WT trimmed and control sides but not KO trimmed and control sides could be distinguished, consistent with what was observed in *Homer1* KOs (**Fig. 7F**). Moreover, SynGAP_PSD95 increased after trimming regardless of genotype, also similar to *Homer1* KOs.

Collectively, these results suggest that a PIN consisting of synaptic scaffolding proteins is integral to the ability of the barrel cortex to maintain homeostasis in response to prolonged sensory deprivation. The observation that many PiSCES that increased after whisker trimming also appeared elevated in the KO barrel cortex basally, before whisker trimming, suggests that loss of function of a major synaptic scaffolding protein may create a "ceiling effect" that prevents synapses from altering their strengths through homeostatic mechanisms, and may explain why whisker trimming has little to no effect on PIN rearrangements in the barrel cortex of mice lacking *Homer1* or *Shank3*. Moreover, such a ceiling effect could operate in both directions. Indeed, NL3_PIKE, the only PiSCES that consistently decreased after whisker trimming in the WT barrel cortex, did not decrease in either KO barrel cortex after trimming and was basally reduced in the barrel cortex of both Kos (**Fig. 7L**).

Discussion

Here we have established a "ground truth" for synaptic protein interactions that transduce prolonged activity perturbations to a homeostatic response. We have demonstrated that *1) prolonged increased or decreased activity of cultured cortical neurons causes widespread bidirectional changes in synaptic PINs*, 2) *most of which appear stable within as little as 12 hours. Several changes, however, may not stabilize until as late as 48 hours. 3) Sensory deprivation by whisker trimming induces a unique homeostatic response in the barrel cortex that 4) requires the synaptic scaffolding proteins Homer1 and Shank3*.

Bidirectional dynamics of upscaling versus downscaling

Homeostatic scaling operates bidirectionally to stabilize cell-wide synaptic strength in response to changes in spiking activity (reviewed in (Turrigiano, 2012)) and/or glutamatergic transmission (Fong et al., 2015), reflected, in part, in bidirectional changes in the synaptic protein content of the postsynaptic density (PSD) (Ehlers, 2003). Here, we have shown that synaptic PINs also change bidirectionally with upscaling and downscaling. While activity perturbation resulted in stable bidirectional PiSCES changes after only 12 hours, almost half of the significant changes for upscaling were not observed until 48 hours, suggesting that some aspects of synaptic scaling are not purely bidirectional. It has been established that upscaling is dependent on transcription (Ibata et al., 2008), that both upscaling and downscaling employ rapid and delayed protein synthesis (Schanzenbächer et al., 2016, 2018), and that translation is required for downscaling *in vivo* (Goold and Nicoll, 2010). Rapid calcium influx prior to downscaling could lead to more immediate transcriptional changes than those triggered by reduced intracellular calcium/CaMKIV phosphorylation prior to upscaling (Ibata et al., 2008). Indeed, blocking calcium channels with $NiCl_2$ or the L-type calcium channel blocker nifepidine was sufficient to produce an upscaling-like response independent of the neuron's ability to fire action potentials (Ibata et al., 2008). Additionally, upscaling is gated by glutamate receptor accumulation at synapses (Gainey et al., 2009), which may prime changes in upscaling throughout the sleep/wake cycle (Hengen et al., 2016). A similar gating function for downscaling has yet to be described. Without a gate, downscaling may therefore proceed rapidly, while upscaling is delayed until a threshold of glutamate has accumulated at synapses. Moreover, while downscaling "fixes" the problem of increased firing, upscaling during prolonged silencing will never restore firing rates until TTX is removed. The extended timecourse of upscaling compared with downscaling *in vitro* could therefore be a result of failure to return to a setpoint during upscaling but not downscaling.

Signal vs. Noise in Signal Transduction Experiments

QMI attempts to measure unstable protein-protein interactions within noisy and stochastic intracellular environments and thus faces reproducibility challenges similar to mass spectrometry (Gonzalez-Lozano et al., 2020; Tabb et al., 2010). While noise is inherent to all signal transduction experiments, we are uniquely able to bioinformatically sort signal from

noise using CNA modules. For example, the "turquoise" module in Figure 3 demonstrates that many true positives are missed by ANC analysis in individual N-of-4 experiments but are clearly identified by CNA with a larger sample size. By contrast, the "brown" module identified PiSCES that change together as a unit, implying an underlying biological origin, but do not correlate with any experimental manipulation, implying biological noise, such as developmental or circadian processes (**Fig. S2**). So why not use an N-of-12 design for all experiments? ANC analysis becomes more stringent with increasing Ns, identifying fewer significant PiSCES for each N over 4 (Smith et al., 2016), while CNA identifies modules of PiSCES that change together, but may not be true positives. Moreover, samples run in parallel show high inter-experimental consistencey (**Fig. S1A**, $R^2 = 0.97$), so by using two statistical tests with independent assumptions (ANC and CAN) and carefully matching biological replicates in each experiment, we are able to identify a subset of the total PiSCES that change in response to a given stimulus using a sample size of 4. Here, in order to understand the full network of rearrangements during homeostatic plasticity, however, we increased the power of CNA by adding more Ns, which reconciles inconsistencies in ANC results between experiments, revealing which ANC hits occur together in a module associated with treatment and which occur together in a module associated with noise.

Homeostatic plasticity *in vitro* versus *in vivo*

Homeostatic synaptic scaling was first demonstrated in neurons cultured from rat visual cortex (Turrigiano et al., 1998). It has since been demonstrated *in vivo* in the visual cortex (Barnes et al., 2017; Desai et al., 2002; Hengen et al., 2013; Keck et al., 2013; Wallace and Bear, 2004) and during sleep (Diering et al., 2017). A recent study, however, demonstrated that visual deprivation by eyelid suture elevates spontaneous activity and lowers the threshold for LTP, a form of homeostatic plasticity distinct from synaptic scaling called "metaplasticity," or the sliding threshold model (Bridi et al., 2018). Similarly, homeostatic plasticity in the barrel cortex after sensory deprivation or GABA agonism is thought to occur not through homeostatic synaptic scaling, but through unequal changes in network excitation and inhibition leading to net increased excitation (Krook-Magnuson and Huntsman, 2005; Li et al., 2014). Silencing input to the barrel cortex, therefore, theoretically results in a counterintuitive downscaling-like response opposite the response to activity blockade *in vitro*. While excitatory blockade *in vitro* was reported to have no effect on excitatory drive onto inhibitory neurons (Turrigiano et al.,

1998), inhibitory neurons nonetheless exhibited increased intrinsic excitability after activity blockade *in vivo* (Desai et al., 1999b). Moreover, homeostatic plasticity in inhibitory circuits *in vivo* appeared to be mediated by specific inhibitory cell types, adding to the vast complexity of *in vivo* mechanisms that maintain firing rates compared with *in vitro* mechanisms (Bartley et al., 2008).

Building on the above studies, we have observed that *in vivo* changes to synaptic PINs in response to sensory deprivation exhibit features of both upscaling and downscaling. This suggests that homeostatic mechanisms *in vivo* may involve both excitatory and inhibitory circuits. It is still unclear, however, if the same PINs that mediate homeostatic synaptic scaling *in vitro* also mediate homeostasis *in vivo,* or if different types of homeostatic plasticity employ different protein complexes and signaling cascades. Our findings thus far lead to an intriguing hypothesis that different forms of homeostatic plasticity employ the same scaffolding proteins, Homer1 and Shank3.

Homeostatic plasticity and ASD

Altered E/I has long been hypothesized to be a unifying mechanism for ASD pathology. The barrel cortex, which receives tactile input from the whiskers, is a particularly appropriate region to model ASD, given that atypical sensory processing and tactile sensitivity are hallmarks of ASD (Goel and Portera-Cailliau, 2019). Several recent reports have suggested that homeostatic plasticity is altered in some ASD syndromes (Bülow et al., 2019; Tatavarty et al., 2018). Given that E/I imbalance is a mechanism for homeostasis in the barrel cortex, it is especially intriguing that several mouse models of ASD exhibit altered homeostasis in the barrel cortex (Antoine et al., 2019), and that deletion of two different ASD genes in mouse peripheral somatosensory neurons resulted in aberrant tactile sensitivity associated with reduced presynaptic inhibition of primary somatosensory neurons (Orefice et al., 2016).

Here, we echo others who have suggested that homeostatic responses of excitatory and inhibitory neurons to prolonged activity perturbation may be altered in some forms of ASD (Antoine et al., 2019). Our finding that mice mutant for the ASD genes *Homer1* or *Shank3* fail to exhibit PIN alterations consistent with a homeostatic response to sensory deprivation supports the theory that disrupted homeostatic plasticity contributes to multiple ASD syndromes.

Moreover, our observation that both *Homer1* and *Shank3* KO mice appear to be molecularly "pre-scaled," or have baseline altered synaptic PINs consistent with sensory deprivation, provides evidence for a "ceiling effect" preventing a homeostatic response to changes in network activity. Collectively, these results support a model whereby diverse ASD phenotypes share the common feature of an inability to restore firing rates to a set-point during prolonged activity perturbation. Indeed, many of the excitatory postsynaptic proteins we have analyzed here are associated with ASD and are involved in the homeostatic response to activity perturbation *in vitro* and *in vivo*. Genetic disruption of any one of these synaptic proteins could alter the neuron's ability to restore homeostasis during periods of prolonged activity perturbation.

Acknowledgments
The authors would like to thank members of the Smith lab, especially Emily Brown, and members of the Center for Integrative Brain Research for helpful discussions.

Funding sources

This work was supported by The National Institute of Health, grants MH102244 and MH113545 (SEPS) and NS31224 (JPW).

Author Contributions

W.E.H. and S.E.P.S designed the study. W.E.H., H.S., J.L., K.I., and E.G. performed the experiments. W.E.H., H.S., J.L., and S.E.P.S. analyzed the data. W.E.H., H.S., and S.E.P.S. wrote the manuscript. S.E.P.S and J.P.W. supervised the project and obtained funding. All authors reviewed the final manuscript.

Abbreviations

AMPA: a-amino-3-hydroxy-5-methyl-4-isoxazolepropionic acid
ANC: Adaptive Nonparametric analysis with an empirical alpha Cutoff
BIC: bicuculine
CAN: Correlation Network Analysis
DIV: days *in vitro*
DMSO: dimethyl sulfoxide
IP: immunoprecipitation
mEPSC: mini excitatory postsynaptic current
MFI: Median Fluorescent Intensity
mGluR: metabotropic glutamate receptor
P0: postnatal day 0
PBS: phosphate buffered saline
PCA: Principal Component Analysis
PiSCES: Proteins in Shared Complexes Detected By Surface Epitopes)
QMI: Quantitative Multiplex Immunoprecipitation
THIP: 4,5,6,7-tetrahydroisoxazolo[5,4-c]pyridine-3-ol
tSNE: t-distributed stochastic neighbor embedding
TTX: tetrototdoxin

Materials and Methods

Animals

All animal work was carried out in compliance with The Seattle Children's Research Institute IACUC under approved protocol #00072 and institutional and federal guidelines. CD-1 and *Homer1*^{tm1Mhd} (stock 023312), and *Shank3*^{tm2Gfng} (stock 017688) mice were originally obtained from The Jackson Laboratory (Bar Harbor, ME).

Genotyping: 0.2 μL of crude DNA extract (KAPA Biosystems) from ear punch tissue was used for genotyping the Homer1^{tm1Mhd} allele with the following primers: 5'-CAA TGC ATG CAA TTC CTG AG-3', 5'-CGA GAA ACT TAC ATA TAT CCG CAA A-3', and 5'-GAA CTT CGC GCT ATA

ACT TCG-3' (The Jackson Laboratory), or the Shank3B$^-$ allele with the following primers: 5'-GAG ACT GAT CAG CGC AGT TG-3', 5'-TGA CAT AAT CGC TGG CAA AG-3', 5'-GCT ATA CGA AGT TAT GTC GAC TAG G-3'.

Cortical Neuron Culture, Surface Labeling, and *Drug Treatment*

Primary cultures of cortical neurons were prepared as previously described (Lautz et al., 2018). Briefly, whole cortex from P0-P1mouse neonates was dissociated using papain (Worthington) and plated at a density of $1.0x10^6$ cells/mL onto 6-well plates treated with poly-D-lysine. Cells were cultured in Neurobasal medium supplemented with 2% B27 and 0.5mM GlutaMax (ThermoFisher) and kept at 37°C, 5% CO_2 for 18-21 days. After 3-5 DIV, 5-fluoro-2'-deoxyuridine was added to a final concentration of 5 μM to inhibit glial proliferation.

For surface labeling of GluR1, cortical cells were dissociated and cultured as above, with the following exceptions: cells were plated at a density of $1.0x10^5$ cells/mL on glass coverslips treated with poly-D-lysine in 24-well plates. A mouse antibody to the N-terminus of GluR1 conjugated with Alexa Fluor 488 (G-12, Santa Cruz Biotechnology) was added to primary neuron cultures (18-21 DIV) to a final concentration of 4μg/mL (1:50 dilution), and cells were kept at 37°C, 5% CO_2 for 20 minutes. Culture medium was then removed, and cells were washed once with 1X PBS and fixed with pre-warmed 4% PFA/4% sucrose in 1XPBS at room temperature for 10 minutes shielded from light. After fixation, cells were washed twice with 1X PBS and mounted on glass slides using ProLong Antifade Mountant with Dapi (Invitrogen). Cells were imaged on a Zeiss LSM 710 at 100X. Mean gray values of 8-bit images were calculated in the green channel after thresholding using default settings in ImageJ. Nine cells from at least 3 independent experiments were included in the final analysis. A paired two-tailed Student's t-Test was used to determine significance.

For *in vitro* homeostatic scaling experiments, TTX (2mM), BIC (40mM), or THIP (20mM) (Tocris) was added directly to the culture medium, and cells were cultured as normal, then lysed after 12, 24, or 48 hours. DMSO (0.4%) served as a vehicle control.

Lysate Preparation

Following treatment of cultured cells, cell culture medium was removed and cells were scraped in cold lysis buffer (150mM NaCl, 50mM Tris pH 7.5, 1% NP-40, 10mM Sodium Fluoride, 2mM sodium orthovanadate, protease inhibitor cocktail (Sigma) and phosphatase inhibitor cocktail (Sigma)), transferred to a centrifuge tube, incubated on ice for 15 minutes, and centrifuged at high seed for 15 minutes to remove nuclei and debris. The protein concentration of the supernatant was determined using a Bradford assay (Pierce).

Lysates from cortical slices were prepared as above with the following exceptions: Adult mice were anesthetized with isoflurane and perfused through the heart with ice cold 1X PBS. Brains were immediately removed, placed into cold PBS, and sliced in cold PBS using a VT1200s vibrating microtome (Leica). Five 500μm slices through the somatosensory (barrel) cortex were divided at the midline into ipsilateral and contralateral hemispheres. All slices from one hemisphere were combined into lysis buffer and mechanically dissociated using a PYREX tissue grinder.

Quantitative Multiplex Immunoprecipitation

QMI was performed as described previously (Lautz et al., 2018; Smith et al., 2016). Briefly, a master mix containing equal numbers of each antibody-coupled Luminex bead was prepared and distributed to lysates containing equal amounts of protein and incubated overnight on a rotator at 4°C. The next day, beads from each sample were washed twice in cold Fly-P buffer (50mM tris pH7.4, 100mM NaCl, 1% bovine serum albumin, and 0.02% sodium azide) and distributed into twice as many wells of a 96-well plate as there were probe antibodies (for technical duplicates). Biotinylated detection (probe) antibodies were added to the appropriate wells and incubated at 4°C with gentle agitation for 1 hour. The resulting bead-probe complexes were washed 3 times with Fly-P buffer, incubated for 30 minutes with streptavidin-PE on ice, washed another 3 times, resuspended in 125μl ice cold Fly-P buffer, and processed for fluorescence using a customized refrigerated Bio-Plex 200 (Smith et al., 2016). Antibody clone names, catalog numbers, and lot numbers are the same as in (Lautz et al., 2018).

Whisker Trimming and THIP administration

Mystacial whiskers on one side of an adult mouse (7-9 weeks) were removed with an electric trimmer while the mouse was under very brief isoflurane anesthesia. Mice were then placed in a clean cage with one familiar cagemate (also unilaterally shaved) for 48 hours. For THIP experiments, either THIP hydrochloride (Tocris) or an equal volume of PBS (vehicle control) was injected intraperitoneally at a concentration of 10mg/kg. Eight hours after the initial injection at the time of trimming, a second injection was given, and two additional injections were given the following day, 8 hours apart, for a total of 4 injections over 48 hours. Lysates were prepared as described above 48 hours after trimming.

Western Blotting

For western blots, proteins (20 μg per lane) were separated by SDS-PAGE and transferred to a PVDF membrane (Millipore). Membranes were blocked in 4% milk in TBST (0.05M Tris pH7.2, 0.15M NaCl, 0.1% Tween20) for 1 hour at room temperature and incubated with primary antibodies overnight at 4°C or for 1 hour at room temperature. Primary antibodies and dilutions used for western blots were Fyn (clone 59, BioLegend, 1:1000), GluR1 (1504, Millipore, 0.001 mg/ml), Homer1 (AT1F3, LSBio, 1:1000), mGluR5 (5675, Millipore, 1:2000), PSD95 (K28/43, BioLegend, 1:500), beta Actin (GTX109639, GeneTex, 1:10,000), phospho-ERK T202/Y204 (4370, Cell Signaling Technologies, 1:1000), and total ERK (9102, Cell Signaling Technologies, 1:1000). Primary antibodies were detected using species-specific HRP-conjugated secondary antibodies. Blots were developed using Femto Maximum Sensitivity Substrate (Pierce) and imaged using a Protein Simple imaging system.

Data Analysis and Statistics

ANC: High-confidence, statistically significant differences in bead distributions between conditions for individual PiSCES, after correcting for multiple comparisons, were identified using ANC as described in (Smith et al., 2016).

CNA: Modules of PiSCES that co-varied with experimental conditions were identified using CNA as described in (Lautz et al., 2018; Smith et al., 2016). Briefly, bead distributions used in ANC were collapsed into a single MFI for every PiSCES and averaged across technical replicates for input into the WGCNA package for R (Langfelder and Horvath, 2008). PiSCES

with MFI < 100 were removed, and batch effects were corrected using COMBAT (Johnson et al., 2007). Power values giving the approximation of scale-free topology were determined using soft thresholding with a power adjacency function. The minimum module size was always set to between 10 and 12, and modules whose eigenvectors significantly correlated with an experimental trait ($p<0.05$) were considered "of interest." PiSCES belonging to module of interest and whose probability of module membership in that module were < 0.05 were considered significantly correlated with that trait. PiSCES that were significant by both ANC and CNA for a given experimental condition were considered significantly altered in that condition.

Hierarchical clustering and PCA: Post-COMBAT, $\log_2$ transformed MFI values were clustered using the hclust function in R with a correlation distance matrix and average clustering method. Approximately unbiased (AU) values were determined using the pvclust package in R. PCA was performed using the prcomp function in R.

t-SNE: Log_2(fold change) values for all PiSCES, or for all PiSCES that were significant in any condition where specified, were encoded in a vector for each condition and dimensionally reduced using PCA. The t-SNE algorithm (Maaten and Hinton, 2008) with perplexity 2 was then used to reduce the vectors to 2 dimensions in R. Hierarchical clustering was used to fit conditions into 4 clusters, which were visualized using ggplot. The most significant PiSCES between treatment groups were determined by Wilcoxon rank-sum pairwise comparisons of sets grouped by treatment, regardless of tSNE cluster, in R.

Data visualization: Nested network (node-edge) diagrams were generated in Cytoscape v3.7.1 (Shannon et al., 2003). The mean $\log_2$(fold change) over control of a given PiSCES from all significant biological replicates (significance determined by ANC) was used to generate each edge. Heatmaps were generated using Heatmap.2 in R.

Electrophysiology

Acute slice preparation: Adult male mice (7-9 weeks old) were anesthetized with isoflurane inhalation anesthetic and perfused through the heart with ice cold standard artificial cerebral spinal fluid (ACSF). Brains were rapidly removed and placed into ice-cold cutting ACSF. 300 µm thalamocortical slices were cut on a VT1000s vibrating microtome (Leica) and were gently warmed to 35^{0}C for 15-20 minutes then allowed cooled to room temperature prior to recording.

Patch clamp recording: All recordings were performed at 32.5 ± 1^{0}C. Barrel cortex LII/III pyramidal neurons were visually identified under DIC optics (Nikon) and confirmed by their electrophysiological profile and *posthoc* morphological reconstruction. Recordings were sampled at 10 KHz with a Multiclamp 700B amplifier Digidata 1400 digitizer (Molecular Devices) and were rejected if $I_{Holding}$ exceeded ± 100 pA from -70 mV in voltage camp or if Vm changed more than 15% in current clamp. Only cells with > 1 GΩ seal and Vm ≤ -55 mV were included in analysis. Junction potential was 13 mV (compensated).

Histology: Neurobiotin was allowed to passively diffuse throughout the dendritic tree for the duration of each recording (>10 minutes). The recording pipette was carefully withdrawn and the membrane allowed to re-seal before separation with a tap to the headstage. The slice was immediately transferred to 4% paraformaldehyde for > 1hr and kept up to 2 weeks at 4^{0}C before processing with streptavidin. PFA was removed with 4 15-minute washes in 1X PBS

and followed with a 2-hr block in 1X PBS + 0.5% Triton X-100 and 10% goat serum. 1% Alexa 488-streptavidin conjugate was added to fresh blocking solution for 1-2 hrs then washed 4X for 15 minutes each in 1X PBS. Slices were mounted with Vectashield anti-fade mounting medium with DAPI (Vector Labs) and visualized on a LSM 710 confocal microscope (Zeiss) with 20X, 40X, and 63X objectives. Spines were counted by an observer blind to hemisphere over a 15-50 μm continuous section of dendrites located 100-150 μm from the cell body.

Solutions and drugs: Standard ACSF (in mM): NaCl 128, KCl 3, NaH_2PO_4 1.25, $NaHCO_3$ 26, Glucose 10, $CaCl_2$ 2, $MgSO_4$ 2; pH 7.35-7.4 and 305-315 mOsm. Cutting ACSF (in mM): Sucrose 75, NaCl 87, KCl 3, NaH_2PO_4 1.25, $NaHCO_3$ 26, Glucose 20, $CaCl_2$ 0.5, $MgSO_4$ 7; pH 7.35-7.4 and 305-315 mOsm. Internal recording solution (in mM): $KmeSO_4$, KCl 7, EGTA 0.1, Na_2ATP 2, MgATP 2, Na_2GTP 0.3, phosphocreatine 5, 0.2% neurobiotin. 7.4 pH, 285-295 mOsm. Bath-applied drugs: Tetrodotoxin 1 μM, picrotoxin 25 μM.

Analysis and statistics: Raw traces were acquired, offline filtered to 1 KHz, and analyzed with the pClamp software suite (v. 10.7, Molecular Devices). Neuron reconstructions were performed using ShuTu dendrite tracing software (http://personal.psu.edu/dzj2/ShuTu/) and the Sholl Analysis plug-in for FIJI/ImageJ (Ferreira et al. Nat Methods 11, 982-4 (2014)). Statistics and plotting were performed with OriginLab Pro 2017.

References

Ango, F., Pin, J.P., Tu, J.C., Xiao, B., Worley, P.F., Bockaert, J., and Fagni, L. (2000). Dendritic and axonal targeting of type 5 metabotropic glutamate receptor is regulated by homer1 proteins and neuronal excitation. J. Neurosci. Off. J. Soc. Neurosci. *20*, 8710–8716.

Antoine, M.W., Langberg, T., Schnepel, P., and Feldman, D.E. (2019). Increased Excitation-Inhibition Ratio Stabilizes Synapse and Circuit Excitability in Four Autism Mouse Models. Neuron *101*, 648-661.e4.

Aoto, J., Nam, C.I., Poon, M.M., Ting, P., and Chen, L. (2008). Synaptic signaling by all-trans retinoic acid in homeostatic synaptic plasticity. Neuron *60*, 308–320.

Barnes, S.J., Franzoni, E., Jacobsen, R.I., Erdelyi, F., Szabo, G., Clopath, C., Keller, G.B., and Keck, T. (2017). Deprivation-Induced Homeostatic Spine Scaling In Vivo Is Localized to Dendritic Branches that Have Undergone Recent Spine Loss. Neuron *96*, 871-882.e5.

Bartley, A.F., Huang, Z.J., Huber, K.M., and Gibson, J.R. (2008). Differential activity-dependent, homeostatic plasticity of two neocortical inhibitory circuits. J. Neurophysiol. *100*, 1983–1994.

Bateup, H.S., Denefrio, C.L., Johnson, C.A., Saulnier, J.L., and Sabatini, B.L. (2013). Temporal dynamics of a homeostatic pathway controlling neural network activity. Front. Mol. Neurosci. *6*.

Benevento, L.A., Bakkum, B.W., Port, J.D., and Cohen, R.S. (1992). The effects of dark-rearing on the electrophysiology of the rat visual cortex. Brain Res. *572*, 198–207.

Bienenstock, E.L., Cooper, L.N., and Munro, P.W. (1982). Theory for the development of neuron selectivity: orientation specificity and binocular interaction in visual cortex. J. Neurosci. *2*, 32–48.

Bridi, M.C.D., de Pasquale, R., Lantz, C.L., Gu, Y., Borrell, A., Choi, S.-Y., He, K., Tran, T., Hong, S.Z., Dykman, A., et al. (2018). Two distinct mechanisms for experience-dependent homeostasis. Nat. Neurosci. *21*, 843–850.

Bülow, P., Murphy, T.J., Bassell, G.J., and Wenner, P. (2019). Homeostatic Intrinsic Plasticity Is Functionally Altered in Fmr1 KO Cortical Neurons. Cell Rep. *26*, 1378-1388.e3.

Cafarelli, T.M., Desbuleux, A., Wang, Y., Choi, S.G., De Ridder, D., and Vidal, M. (2017). Mapping, modeling, and characterization of protein-protein interactions on a proteomic scale. Curr. Opin. Struct. Biol. *44*, 201–210.

Cai, C., Li, H., Rivera, C., and Keinänen, K. (2006). Interaction between SAP97 and PSD-95, two Maguk proteins involved in synaptic trafficking of AMPA receptors. J. Biol. Chem. *281*, 4267–4273.

Chowdhury, S., Shepherd, J.D., Okuno, H., Lyford, G., Petralia, R.S., Plath, N., Kuhl, D., Huganir, R.L., and Worley, P.F. (2006). Arc Interacts with the Endocytic Machinery to Regulate AMPA Receptor Trafficking. Neuron *52*, 445–459.

Desai, N.S., Rutherford, L.C., and Turrigiano, G.G. (1999a). Plasticity in the intrinsic excitability of cortical pyramidal neurons. Nat. Neurosci. *2*, 515–520.

Desai, N.S., Rutherford, L.C., and Turrigiano, G.G. (1999b). BDNF regulates the intrinsic excitability of cortical neurons. Learn. Mem. Cold Spring Harb. N *6*, 284–291.

Desai, N.S., Cudmore, R.H., Nelson, S.B., and Turrigiano, G.G. (2002). Critical periods for experience-dependent synaptic scaling in visual cortex. Nat. Neurosci. *5*, 783–789.

Diering, G.H., Gustina, A.S., and Huganir, R.L. (2014). PKA-GluA1 Coupling via AKAP5 Controls AMPA Receptor Phosphorylation and Cell-Surface Targeting during Bidirectional Homeostatic Plasticity. Neuron *84*, 790–805.

Diering, G.H., Nirujogi, R.S., Roth, R.H., Worley, P.F., Pandey, A., and Huganir, R.L. (2017). Homer1a drives homeostatic scaling-down of excitatory synapses during sleep. Science *355*, 511–515.

Drasbek, K.R., and Jensen, K. (2006). THIP, a hypnotic and antinociceptive drug, enhances an extrasynaptic GABAA receptor-mediated conductance in mouse neocortex. Cereb. Cortex N. Y. N 1991 *16*, 1134–1141.

Ehlers, M.D. (2003). Activity level controls postsynaptic composition and signaling via the ubiquitin-proteasome system. Nat. Neurosci. *6*, 231–242.

Fong, M., Newman, J.P., Potter, S.M., and Wenner, P. (2015). Upward synaptic scaling is dependent on neurotransmission rather than spiking. Nat. Commun. *6*.

Gainey, M.A., Hurvitz-Wolff, J.R., Lambo, M.E., and Turrigiano, G.G. (2009). Synaptic Scaling Requires the GluR2 Subunit of the AMPA Receptor. J. Neurosci. *29*, 6479–6489.

Gainey, M.A., Tatavarty, V., Nahmani, M., Lin, H., and Turrigiano, G.G. (2015). Activity-dependent synaptic GRIP1 accumulation drives synaptic scaling up in response to action potential blockade. Proc. Natl. Acad. Sci. U. S. A. *112*, E3590-3599.

Gainey, M.A., Wolfe, R., Pourzia, O., and Feldman, D.E. (2016). Whisker Deprivation Drives Two Phases of Inhibitory Synapse Weakening in Layer 4 of Rat Somatosensory Cortex. PloS One *11*, e0148227.

Gainey, M.A., Aman, J.W., and Feldman, D.E. (2018). Rapid Disinhibition by Adjustment of PV Intrinsic Excitability during Whisker Map Plasticity in Mouse S1. J. Neurosci. Off. J. Soc. Neurosci. *38*, 4749–4761.

Glazewski, S., Greenhill, S., and Fox, K. (2017). Time-course and mechanisms of homeostatic plasticity in layers 2/3 and 5 of the barrel cortex. Philos. Trans. R. Soc. Lond. B. Biol. Sci. *372*.

Goel, A., and Lee, H.-K. (2007). Persistence of Experience-Induced Homeostatic Synaptic Plasticity through Adulthood in Superficial Layers of Mouse Visual Cortex. J. Neurosci. *27*, 6692–6700.

Goel, A., and Portera-Cailliau, C. (2019). Autism in the Balance: Elevated E-I Ratio as a Homeostatic Stabilization of Synaptic Drive. Neuron *101*, 543–545.

Gonzalez-Lozano, M.A., Koopmans, F., Sullivan, P.F., Protze, J., Krause, G., Verhage, M., Li, K.W., Liu, F., and Smit, A.B. (2020). Stitching the synapse: Cross-linking mass spectrometry into resolving synaptic protein interactions. Sci. Adv. *6*.

Goold, C.P., and Nicoll, R.A. (2010). Single-cell optogenetic excitation drives homeostatic synaptic depression. Neuron *68*, 512–528.

Gray, N.W., Weimer, R.M., Bureau, I., and Svoboda, K. (2006). Rapid Redistribution of Synaptic PSD-95 in the Neocortex In Vivo. PLOS Biol. *4*, e370.

Gygi, S.P., Rochon, Y., Franza, B.R., and Aebersold, R. (1999). Correlation between protein and mRNA abundance in yeast. Mol. Cell. Biol. *19*, 1720–1730.

Hengen, K.B., Lambo, M.E., Van Hooser, S.D., Katz, D.B., and Turrigiano, G.G. (2013). Firing rate homeostasis in visual cortex of freely behaving rodents. Neuron *80*, 335–342.

Hengen, K.B., Torrado Pacheco, A., McGregor, J.N., Van Hooser, S.D., and Turrigiano, G.G. (2016). Neuronal Firing Rate Homeostasis Is Inhibited by Sleep and Promoted by Wake. Cell *165*, 180–191.

Hu, J.-H., Park, J.M., Park, S., Xiao, B., Dehoff, M.H., Kim, S., Hayashi, T., Schwarz, M.K., Huganir, R.L., Seeburg, P.H., et al. (2010). Homeostatic Scaling Requires Group I mGluR Activation Mediated by Homer1a. Neuron *68*, 1128–1142.

Ibata, K., Sun, Q., and Turrigiano, G.G. (2008). Rapid synaptic scaling induced by changes in postsynaptic firing. Neuron *57*, 819–826.

Jewett, K.A., Lee, K.Y., Eagleman, D.E., Soriano, S., and Tsai, N.-P. (2018). Dysregulation and restoration of homeostatic network plasticity in fragile X syndrome mice. Neuropharmacology *138*, 182–192.

Jin, D.-Z., Mao, L.-M., and Wang, J.Q. (2017). An Essential Role of Fyn in the Modulation of Metabotropic Glutamate Receptor 1 in Neurons. ENeuro *4*, ENEURO.0096-17.2017.

Johnson, W.E., Li, C., and Rabinovic, A. (2007). Adjusting batch effects in microarray expression data using empirical Bayes methods. Biostat. Oxf. Engl. *8*, 118–127.

Jovanovic, M., Rooney, M.S., Mertins, P., Przybylski, D., Chevrier, N., Satija, R., Rodriguez, E.H., Fields, A.P., Schwartz, S., Raychowdhury, R., et al. (2015). Immunogenetics. Dynamic profiling of the protein life cycle in response to pathogens. Science *347*, 1259038–1259038.

Keck, T., Keller, G.B., Jacobsen, R.I., Eysel, U.T., Bonhoeffer, T., and Hübener, M. (2013). Synaptic scaling and homeostatic plasticity in the mouse visual cortex in vivo. Neuron *80*, 327–334.

Kirkwood, A., Rioult, M.C., and Bear, M.F. (1996). Experience-dependent modification of synaptic plasticity in visual cortex. Nature *381*, 526–528.

Knogler, L.D., Liao, M., and Drapeau, P. (2010). Synaptic Scaling and the Development of a Motor Network. J. Neurosci. *30*, 8871–8881.

Knott, G.W., Quairiaux, C., Genoud, C., and Welker, E. (2002). Formation of dendritic spines with GABAergic synapses induced by whisker stimulation in adult mice. Neuron *34*, 265–273.

Kotak, V.C., Fujisawa, S., Lee, F.A., Karthikeyan, O., Aoki, C., and Sanes, D.H. (2005). Hearing Loss Raises Excitability in the Auditory Cortex. J. Neurosci. Off. J. Soc. Neurosci. *25*, 3908–3918.

Krook-Magnuson, E.I., and Huntsman, M.M. (2005). Excitability of cortical neurons depends upon a powerful tonic conductance in inhibitory networks. Thalamus Relat. Syst. *3*, 115–120.

Kuhlman, S.J., Olivas, N.D., Tring, E., Ikrar, T., Xu, X., and Trachtenberg, J.T. (2013). A disinhibitory microcircuit initiates critical-period plasticity in the visual cortex. Nature *501*, 543–546.

Langfelder, P., and Horvath, S. (2008). WGCNA: an R package for weighted correlation network analysis. BMC Bioinformatics *9*, 559.

Lautz, J.D., Brown, E.A., Williams VanSchoiack, A.A., and Smith, S.E.P. (2018). Synaptic activity induces input-specific rearrangements in a targeted synaptic protein interaction network. J. Neurochem. *146*, 540–559.

Lautz, J.D., Gniffke, E.P., Brown, E.A., Immendorf, K.B., Mendel, R.D., and Smith, S.E.P. (2019). Activity-dependent changes in synaptic protein complex composition are consistent in different detergents despite differential solubility. Sci. Rep. *9*, 10890.

Li, L., Gainey, M.A., Goldbeck, J.E., and Feldman, D.E. (2014). Rapid homeostasis by disinhibition during whisker map plasticity. Proc. Natl. Acad. Sci. U. S. A. *111*, 1616–1621.

Maaten, L. van der, and Hinton, G. (2008). Visualizing Data using t-SNE. J. Mach. Learn. Res. *9*, 2579–2605.

Mao, W., Salzberg, A.C., Uchigashima, M., Hasegawa, Y., Hock, H., Watanabe, M., Akbarian, S., Kawasawa, Y.I., and Futai, K. (2018). Activity-Induced Regulation of Synaptic Strength through the Chromatin Reader L3mbtl1. Cell Rep. *23*, 3209–3222.

Michaelson, S.D., Ozkan, E.D., Aceti, M., Maity, S., Llamosas, N., Weldon, M., Mizrachi, E., Vaissiere, T., Gaffield, M.A., Christie, J.M., et al. (2018). SYNGAP1 heterozygosity disrupts sensory processing by reducing touch-related activity within somatosensory cortex circuits. Nat. Neurosci. *21*, 1–13.

Nakazawa, T., Komai, S., Tezuka, T., Hisatsune, C., Umemori, H., Semba, K., Mishina, M., Manabe, T., and Yamamoto, T. (2001). Characterization of Fyn-mediated tyrosine phosphorylation sites on GluR epsilon 2 (NR2B) subunit of the N-methyl-D-aspartate receptor. J. Biol. Chem. *276*, 693–699.

O'Brien, R.J., Kamboj, S., Ehlers, M.D., Rosen, K.R., Fischbach, G.D., and Huganir, R.L. (1998). Activity-dependent modulation of synaptic AMPA receptor accumulation. Neuron *21*, 1067–1078.

Orefice, L.L., Zimmerman, A.L., Chirila, A.M., Sleboda, S.J., Head, J.P., and Ginty, D.D. (2016). Peripheral Mechanosensory Neuron Dysfunction Underlies Tactile and Behavioral Deficits in Mouse Models of ASDs. Cell *166*, 299–313.

Peça, J., Feliciano, C., Ting, J.T., Wang, W., Wells, M.F., Venkatraman, T.N., Lascola, C.D., Fu, Z., and Feng, G. (2011). Shank3 mutant mice display autistic-like behaviours and striatal dysfunction. Nature *472*, 437–442.

Phelan, K., and McDermid, H.E. (2012). The 22q13.3 Deletion Syndrome (Phelan-McDermid Syndrome). Mol. Syndromol. *2*, 186–201.

Pozo, K., and Goda, Y. (2010). Unraveling mechanisms of homeostatic synaptic plasticity. Neuron *66*, 337–351.

Rasmussen, A.H., Rasmussen, H.B., and Silahtaroglu, A. (2017). The DLGAP family: neuronal expression, function and role in brain disorders. Mol. Brain *10*, 43–43.

Schanzenbächer, C.T., Sambandan, S., Langer, J.D., and Schuman, E.M. (2016). Nascent Proteome Remodeling following Homeostatic Scaling at Hippocampal Synapses. Neuron *92*, 358–371.

Schanzenbächer, C.T., Langer, J.D., and Schuman, E.M. (2018). Time- and polarity-dependent proteomic changes associated with homeostatic scaling at central synapses. ELife *7*.

Schaukowitch, K., Reese, A.L., Kim, S.-K., Kilaru, G., Joo, J.-Y., Kavalali, E.T., and Kim, T.-K. (2017). An Intrinsic Transcriptional Program Underlying Synaptic Scaling during Activity Suppression. Cell Rep. *18*, 1512–1526.

Shannon, P., Markiel, A., Ozier, O., Baliga, N.S., Wang, J.T., Ramage, D., Amin, N., Schwikowski, B., and Ideker, T. (2003). Cytoscape: a software environment for integrated models of biomolecular interaction networks. Genome Res. *13*, 2498–2504.

Smith, S.E.P., Neier, S.C., Reed, B.K., Davis, T.R., Sinnwell, J.P., Eckel-Passow, J.E., Sciallis, G.F., Wieland, C.N., Torgerson, R.R., Gil, D., et al. (2016). Multiplex matrix network analysis of protein complexes in the human TCR signalosome. Sci. Signal. *9*, rs7.

Steinmetz, C.C., Tatavarty, V., Sugino, K., Shima, Y., Joseph, A., Lin, H., Rutlin, M., Lambo, M., Hempel, C.M., Okaty, B.W., et al. (2016). Upregulation of µ3A Drives Homeostatic Plasticity by Rerouting AMPAR into the Recycling Endosomal Pathway. Cell Rep. *16*, 2711–2722.

Styr, B., and Slutsky, I. (2018). Imbalance between firing homeostasis and synaptic plasticity drives early-phase Alzheimer's disease. Nat. Neurosci. *21*, 463–473.

Sun, Q., and Turrigiano, G.G. (2011). PSD-95 and PSD-93 Play Critical But Distinct Roles in Synaptic Scaling Up and Down. J. Neurosci. *31*, 6800–6808.

Tabb, D.L., Vega-Montoto, L., Rudnick, P.A., Variyath, A.M., Ham, A.-J.L., Bunk, D.M., Kilpatrick, L.E., Billheimer, D.D., Blackman, R.K., Cardasis, H.L., et al. (2010). Repeatability and Reproducibility in Proteomic Identifications by Liquid Chromatography—Tandem Mass Spectrometry. J. Proteome Res. *9*, 761.

Tatavarty, V., Pacheco, A.T., Lin, H., Miska, N.J., Hengen, K.B., Wagner, F.F., and Turrigiano, G.G. (2018). Autism-associated Shank3 is essential for homeostatic plasticity and neuronal circuit stability. BioRxiv 365445.

Trepanier, C.H., Jackson, M.F., and MacDonald, J.F. (2012). Regulation of NMDA receptors by the tyrosine kinase Fyn. FEBS J. *279*, 12–19.

Tu, J.C., Xiao, B., Naisbitt, S., Yuan, J.P., Petralia, R.S., Brakeman, P., Doan, A., Aakalu, V.K., Lanahan, A.A., Sheng, M., et al. (1999). Coupling of mGluR/Homer and PSD-95 complexes by the Shank family of postsynaptic density proteins. Neuron *23*, 583–592.

Turrigiano, G. (2011). Too Many Cooks? Intrinsic and Synaptic Homeostatic Mechanisms in Cortical Circuit Refinement. Annu. Rev. Neurosci. *34*, 89–103.

Turrigiano, G. (2012). Homeostatic synaptic plasticity: local and global mechanisms for stabilizing neuronal function. Cold Spring Harb. Perspect. Biol. *4*, a005736.

Turrigiano, G.G., Leslie, K.R., Desai, N.S., Rutherford, L.C., and Nelson, S.B. (1998). Activity-dependent scaling of quantal amplitude in neocortical neurons. Nature *391*, 892–896.

Wallace, W., and Bear, M.F. (2004). A morphological correlate of synaptic scaling in visual cortex. J. Neurosci. Off. J. Soc. Neurosci. *24*, 6928–6938.

Wilson, H.L., Wong, A.C.C., Shaw, S.R., Tse, W.-Y., Stapleton, G.A., Phelan, M.C., Hu, S., Marshall, J., and McDermid, H.E. (2003). Molecular characterisation of the 22q13 deletion syndrome supports the role of haploinsufficiency of SHANK3/PROSAP2 in the major neurological symptoms. J. Med. Genet. *40*, 575–584.

Yang, M., and Leonard, J.P. (2001). Identification of mouse NMDA receptor subunit NR2A C-terminal tyrosine sites phosphorylated by coexpression with v-Src. J. Neurochem. *77*, 580–588.

Yuan, J.P., Kiselyov, K., Shin, D.M., Chen, J., Shcheynikov, N., Kang, S.H., Dehoff, M.H., Schwarz, M.K., Seeburg, P.H., Muallem, S., et al. (2003). Homer binds TRPC family channels and is required for gating of TRPC1 by IP3 receptors. Cell *114*, 777–789.

Figure Legends

Table 1. Protein targets that comprise the QMI assay, their gene names, protein names, and function.

Figure 1. Prolonged increased or decreased activity of cultured cortical neurons results in network-level changes to multiprotein complexes. (A) Surface GluR1 (green) and Dapi (nuclei, blue) in cortical neurons treated with DMSO (control), BIC or TTX. Mean intensity of GluR1 relative to control (grey) is quantified to the right for BIC (blue) and TTX (orange) (N=9 cells from 3 biological replicates). **(B,C)** Representative western blots of total levels of select synaptic proteins after 24 (B) or 48 (C) hours of DMSO, TTX, or BIC treatment of cultured cortical neurons. Mean protein levels relative to control (grey) after treatment with BIC (blue) or TTX (orange) are shown to the right (N=6 biological replicates). **(D)** Representative western blots of total levels of ERK1/2 and phospho-ERK1/2 after 24 or 48 hours of DMSO, TTX, or BIC treatment. Mean ratios of phospho-ERK to total ERK are shown below (N=3 biological replicates). **(E)** Schematic of workflow for *in vitro* QMI. **(F)** Hierarchical clustering (left) and Principal Component Analysis (PCA, right) of MFI values from 4 independent 48-hour treatments show segregation of TTX, BIC, and DMSO conditions. Error bars represent SD. (*) *P*-value < 0.05; (**) *P*-value < 0.01.

Figure 2. Multiprotein complexes change bidirectionally as a result of prolonged increased or decreased activity *in vitro*. (A) Topological overlap dissimilarity matrix (TOM) plot of all PiSCES (MFI > 100) showing two modules that are significantly correlated with treatment (turquoise and brown squares). **(B)** Module-trait relationship heatmap showing the correlation (top number) and *P* value for each module-trait pair. **(C)** Heatmap of row-normalized MFIs of all ANC-significant PiSCES in the turquoise module after 48 hours of DMSO, TTX, or BIC treatment for four biological replicates. Samples on the X-axis are arranged by naïve hierarchical clustering. PiSCES on they Y-axis are arranged into those that go up with TTX/down with BIC and vice versa. For each IP_probe combination, the IP protein is always on the left, and the probe is always on the right. Black boxes denote which PiSCES were significantly altered after each treatment (by ANC). Nested networks of the mean $\log_2$(fold change) for each condition for each ANC-significant PiSCES in the turquoise module are to the right of the heatmap. Every protein analyzed as an IP or probe is a single node. The width and the saturation of each edge correlates with the magnitude of the difference from control. Red indicates increased association, and blue indicates decreased association. **(D)** Heatmap of row-normalized MFIs of all ANC-significant PiSCES in the brown module, with samples on the X-axis arranged by naïve hierarchical clustering. Nested networks of the ANC-significnat PiSCES in the brown module are to the right of the heatmap.

Figure 3. **QMI detects a subset of high-confidence PiSCES changes during *in vitro* upscaling and downscaling. (A)** Venn diagrams showing the overlap of significant PiSCES changes for each of three independent sets of experiments ("sets"; N=4 or 5 biological replicates per set). **(B)** Module-trait relationship heatmap showing the correlation (top number) and *P* value for each module-trait pair (N=13 biological replicates). **(C)** Heatmap of row-normalized MFIs of all ANC-significant PiSCES in the turquoise module. Samples on the X-axis are arranged by naïve hierarchical clustering. PiSCES on they Y-axis are arranged into those that go up with TTX/down with BIC and vice versa. **(D)** Bar graphs of the mean $\log_2$(fold change) of select PiSCES after 48 hours of TTX (orange) or BIC (blue) treatment for each set.

PiSCES in pink in C are represented by bar graph in D. Pink asterices indicate that the result was significant in the set. Regardless of significance, mean $\log_2$(fold changes) broadly trended the same direction for each set.

Figure 4. Many PiSCES changes stabilize within 12 hours of homeostatic scaling, while some changes are not detectable until between 24 and 48 hours. (A) Heirarchical clustering of three sets of experiments (N=4 per set) covering three time points (12 hours, 24 hours, and 48 hours) shows separation of all 12 TTX samples into one significant cluster, regardless of time, while BIC and DMSO samples form distinct sub-clusters. AU *P* values are shown in red. **(B)** PCA of all PiSCES measurments (MFI>100) from the three sets shows separation of TTX and BIC conditions along PC1 for each of 3 time points (12 hrs, 24 hrs, 48 hrs). **(C)** Module-trait relationship heatmap showing the correlation (top number) and *P*-value for each module-trait pair (N=12 biological replicates). **(D)** Venn diagrams showing the overlap of significant PiSCES changes for each of the three independent sets. **(E)** Row-normalized heatmaps of the mean $\log_2$(fold change) after 12, 24, and 48 hrs of TTX or BIC treatment for every ANC-significant PiSCES represented in the turquoise module. DMSO is set to 0 (not shown), so that blues indicate decreased interaction, and reds indicate increased interaction. Dark outlines indicate the time points at which the PiSCES measurement was significantly different from DMSO, and PiSCES are arranged into groups according to the earliest time point at which they became significant.

Figure 5. Whisker trimming causes increased synaptic activity in L2/3 pyramidal neurons of the contralateral barrel cortex. (A) Workflow schematic for sensory deprivation and analysis of somatosensory (barrel) cortex. **(B,C)** Mean frequency (B) and amplitude (C) of mEPSCs in the ipsilateral (black) and contralateral (red) barrel cortex. **(D)** 20s raw traces from ipsilateral (top, black) and contralateral (bottom, red) hemispheres. Scale bar: 10pA, 2s. **(E)** Cumulative probability of inter-event intervals (0-2s, 0.1s bins). **(F)** Cumulative probability of mEPSC amplitudes (0-30pA, 2pA bins). **(G)** Mean synaptic spine density at 100-150 μm from the soma. Confocal images of neurobiotin-filled L2/3 ipsilateral (top) and contralateral (bottom) dendrites. Ipsilateral: $N = 9$, Contralateral: $N = 12$. Scale bar = 10 μm. **(H)** PCA of all PiSCES (mean MFI > 100) from 4 control (ipsilateral, black) and 4 trimmed (contralateral, red) hemispheres. **(I)** Hierarchical clustering of 4 control and 4 trimmed hemispheres using all PiSCES (mean MFI > 100). AU *P* values are shown in red. **(J)** Heatmap of row-normalized MFI of all PiSCES significantly altered after whisker trimming.

Figure 6. PiSCES changes during whisker trimming are unique to whisker trimming. (A) Heatmap of row-normalized MFI of all high-confidence *in vivo* PiSCES in control and trimmed samples (N=14 per condition). Samples on the x-axis are arranged by hierarchical clustering. **(B)** Chart comparing the direction of change of high-confidence *in vivo* PiSCES after trimming with the direction of change (if any) after upscaling and downscaling. Red indicates increased interaction, blue indicates decreased, and white indicates that the PiSCES did not change significantly. **(C)** tSNE of *in vitro* upscaling, *in vitro* downscaling, *in vivo* whisker trimming, and THIP treatment using mean $\log_2$(fold change) of all PiSCES significantly altered after TTX, BIC, THIP, or whisker trimming. Each sample input into tSNE represents a single set (N=4 biological replicates per set). **(D)** Box-and-whisker plots of select PiSCES that behaved differently between *in vitro* upscaling, *in vitro* downscaling, and *in vivo* whisker trimming.

Figure 7. Homeostatic plasticity is disrupted in the barrel cortex of mice mutant for *Homer1* or *Shank3*. (A, B) PCA of all PiSCES (mean MFI>100) from 4 biological replicates from sensory-deprived and control hemispheres of *Homer1* WT (red/trimmed vs. black/not trimmed) and *Homer1* KO (purple/trimmed vs. blue/not trimmed) (A) or *Shank3B* WT (grey/trimmed vs. salmon/not trimmed) and *Shank3B* KO (green/trimmed vs. turquoise/not trimmed) (B) adult mice. **(C, E)** Heatmap of row-normalized MFI of all ANC-significant PiSCES after whisker trimming or between WT and KO controls for the *Homer1* set (C) and the *Shank3B* set (E). **(D, F)** Heatmaps of row-normalized MFI of all ANC-significant PiSCES altered only after whisker trimming in WT or KO mice separated into WT and KO specific heatmaps for the *Homer1* set (D) and the *Shank3B* set (F). **(G-L)** Bar graphs of mean $\log_2$(fold changes) of select PiSCES after whisker trimming in control and KO barrel cortex (red/*Homer1* WT vs. purple/*Homer1* KO; salmon/*Shank3B* WT vs. green/*Shank3B* KO, N=6,4,4,4, respectively) along with baseline differences between WT and KO controls (blue/*Homer1* KO vs. WT and turquoise/*Shank3B* KO vs. WT, N=4,4). The effect of whisker trimming on the *Homer1* set is on the left, the *Shank3B* set is in the middle, and baseline genotypic differences are on the right. A red asterisk indicates that the PiSCES was ANC-significant for that condition. A black asterisk indicates that the PiSCES was ANC∩CAN-significant for the full WT set (N=14). For C-F, PiSCES that are ANC∩CNA-signficant (N=14) are in bold. PiSCES in red are graphed in G-L.

Table S1. Mean log2(fold change) of MFI of PiSCES significantly altered by 48 hours of *in virto* TTX, BIC, or both.

Table S2. Top-ranked significantly different PiSCES between three models of homeostatic plasticity (Wilcoxon rank-sum test). PiSCES in bold are significantly different between the *in vivo* model and both *in vitro* models. N=7 sets (TTX), 7 sets (BIC), and 4 sets (Trim), 4 biological replicates per set.

Fig. S1. Parallel experiments show high concordance. (A, B) Mean log2(fold change) of all PiSCES that changed significantly in at least one of the two sets of experiments being compared. Each set was run in parallel (on the same QMI plate, for cultures grown at the same time). Sets under a single treatment condition (TTX1 vs. TTX2) showed high concordance (A), while sets run in parallel but exposed to different treatment conditions (TTX1 vs. BIC1) showed low concordance (B).

Fig. S2. Expaned TOM clustering dendrogram. The 'turquoise' bidirectional module from the N-of-12 *in vitro* analysis contains high-confidence PiSCES that change after 48 hours of upscaling or downscaling. The TOM-clustering dendrogram of PiSCES, with ANC-significant PiSCES labels colored turquoise, is shown above a heatmap of row-normalized MFIs of all ANC-significant PiSCES. In contrast, the brown module also contains ANC-significant PiSCES highlighted in brown, but the heatmap of row-normalized MFIs does not show a clear relationship beteen PiSCES intensity and treatment, suggesting 'brown' is a noise module. Samples on the Y-axis are arranged by treatment, and PiSCES on the X-axis are arranged in the order they appear on the dendrogram.

Fig. S3. QMI detects a subset of high-confidence PiSCES changes during *in vivo* homeostatic plasticity. (A) Heirarchical clustering of 14 biological replicates shows segregation of control and trimmed hemispheres into significantly different clusters. AU *p*-values are shown in red. **(B)** Module-trait relationship heatmap showing the correlation (top

number) and *P*-value for each module-trait pair (N=14 biological replicates). **(C)** TOM-clustering dendrogram of PiSCES arranged above their primary modules, with heatmaps of row-normalized MFIs of all ANC-significant PiSCES in the brown (far left), yellow (left of center), turquoise (right of center), blue (right), or green (far right) module. Samples on the Y-axis are arranged by treatment except for the far left heatmap, in which they are arranged by hemisphere.

Fig. S4. THIP treatment causes synaptic protein rearrangements that are distinct from *in vitro* homeostatic synaptic scaling and *in vivo* whisker deprivation. (A) PCA of all PiSCES measurements (MFI>100) after 48 hours of DMSO (control), TTX, BIC, or THIP treatment of cultured cortical neurons. **(B)** PCA of all PiSCES measurements (MFI>100) in the barrel cortex after 48 hours of PBS alone, PBS plus whisker trimming, THIP alone, and THIP plus whisker trimming.

QMI Name	Gene Name	Protein Name	Function
Scaffolding Proteins			
Homer1	Homer1	Homer protein homolog 1	Scaffold
panShank	Shank1, Shank2, Shank3	SH3 and multiple ankyrin repeat domains protein	Scaffold
panHomer	Homer1, Homer2, Homer3	Homer protein homolog	Scaffold
PSD95	DLG4	Disks large homolog 4	MAGUK Scaffold
SAP97	DLG1	Disks large homolog 1	MAGUK Scaffold
SAPAP	DLGAP1	Disks large-associated protein 1	Scaffold
Shank1	Shank1	SH3 and multiple ankyrin repeat domains protein 1	Scaffold
Shank3	Shank3	SH3 and multiple ankyrin repeat domains protein 3	Scaffold
Glutamate Receptors			
GluR1	Gria1	Glutamate receptor 1	Receptor
GluR2	Gria2	Glutamate receptor 2	Receptor
NMDAR1	Grin1	Glutamate receptor ionotropic, NMDA 1	Receptor
NMDAR2A	Grin2a	Glutamate receptor ionotropic, NMDA 2A	Receptor
NMDAR2B	Grin2b	Glutamate receptor ionotropic, NMDA 2B	Receptor
mGluR5	Grm5	Metabotropic glutamate receptor 5	Receptor
Signal Transducers			
CaMKII	CaMKII	Calcium/calmodulin-dependent protein kinase type II alpha chain	Kinase
Fyn	Fyn	Tyrosine-protein kinase Fyn	Kinase
Homer1a	Homer1	Immediate early gene protein Homer1A	Immediate early gene
NL3	NLGN3	Neuroligin-3	Cell adhesion
PI3K	Pik3ca	Phosphatidylinositol 4,5-bisphosphate 3-kinase catalytic subunit alpha	Kinase
PIKE	Agap2	Arf-GAP with GTPase, ANK repeat and PH domain-containing protein 2	GTPase
SynGAP	Syngap1	Ras/Rap GTPase-activating protein SynGAP	GTPase-activating protein
Ube3a	Ube3a	Ubiquitin-protein ligase E3A	Ubiquitin ligase

Table 1. Protein targets that comprise the QMI assay, their gene names, protein names, and functions.

Figure 1

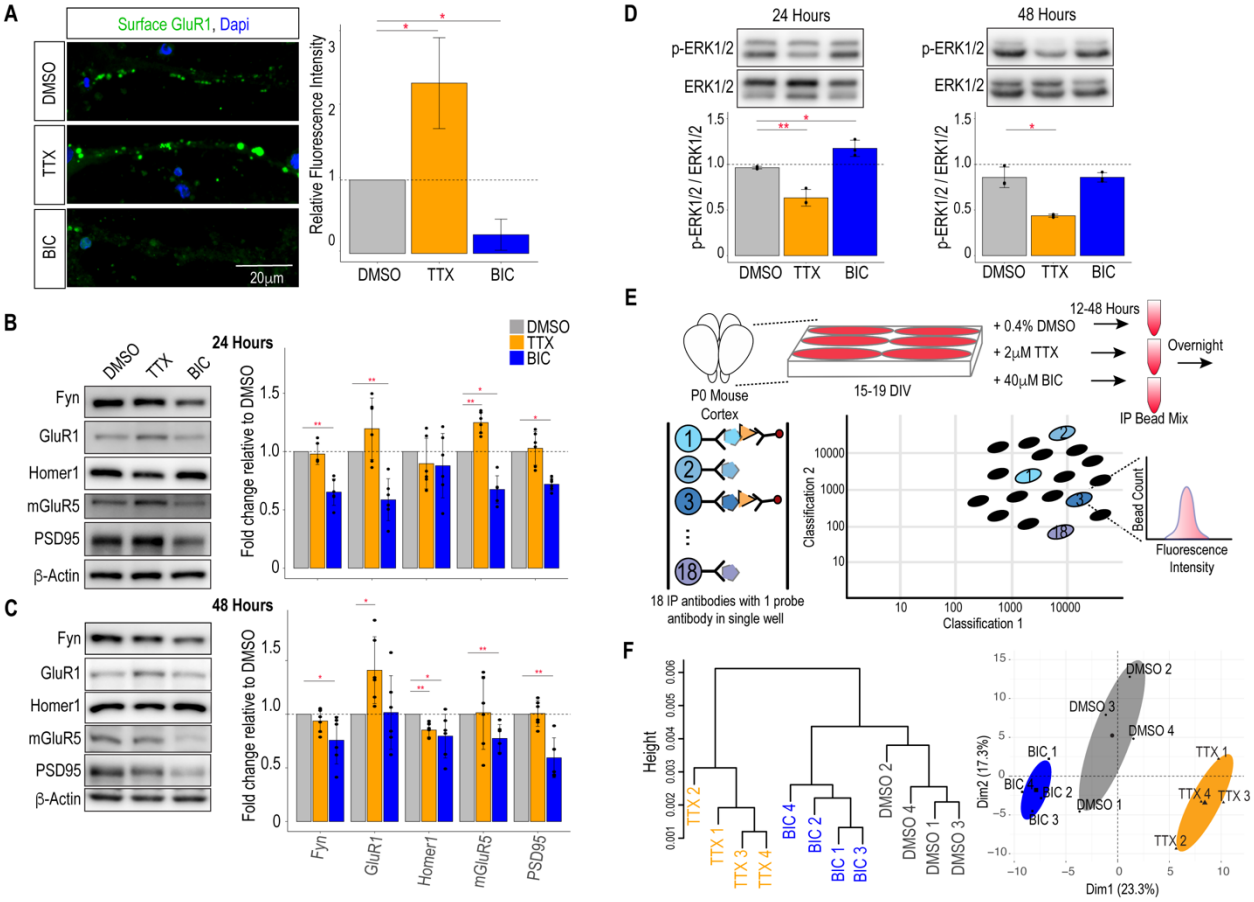

Figure 2

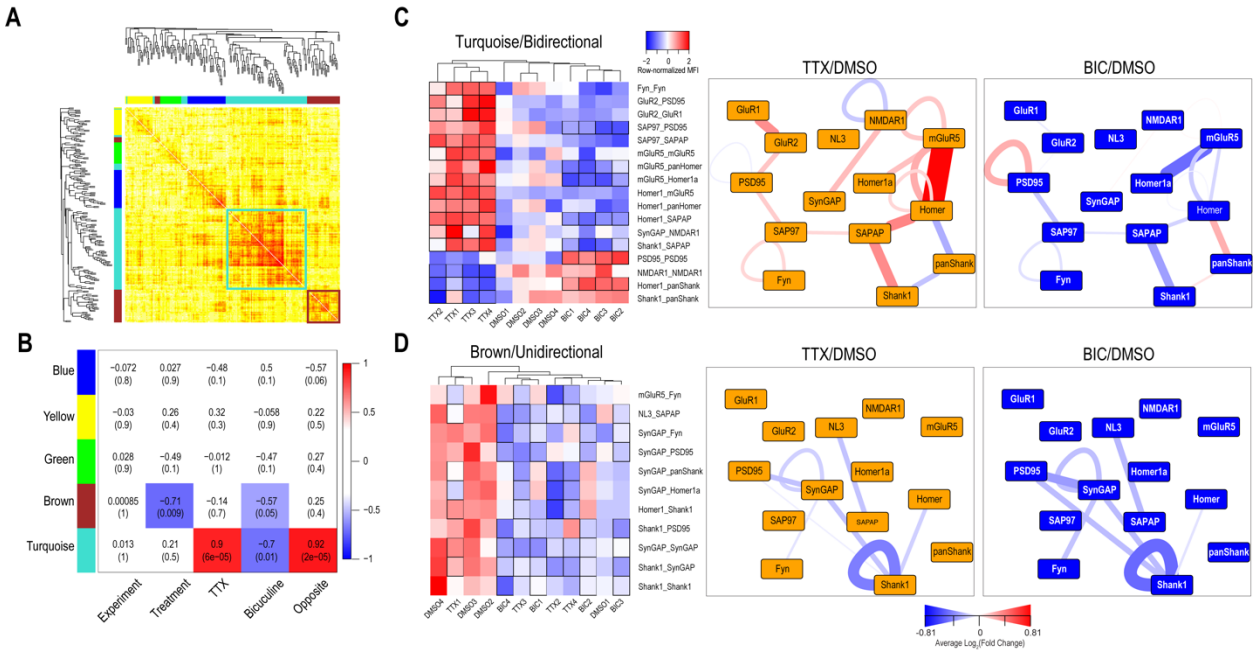

Figure 3

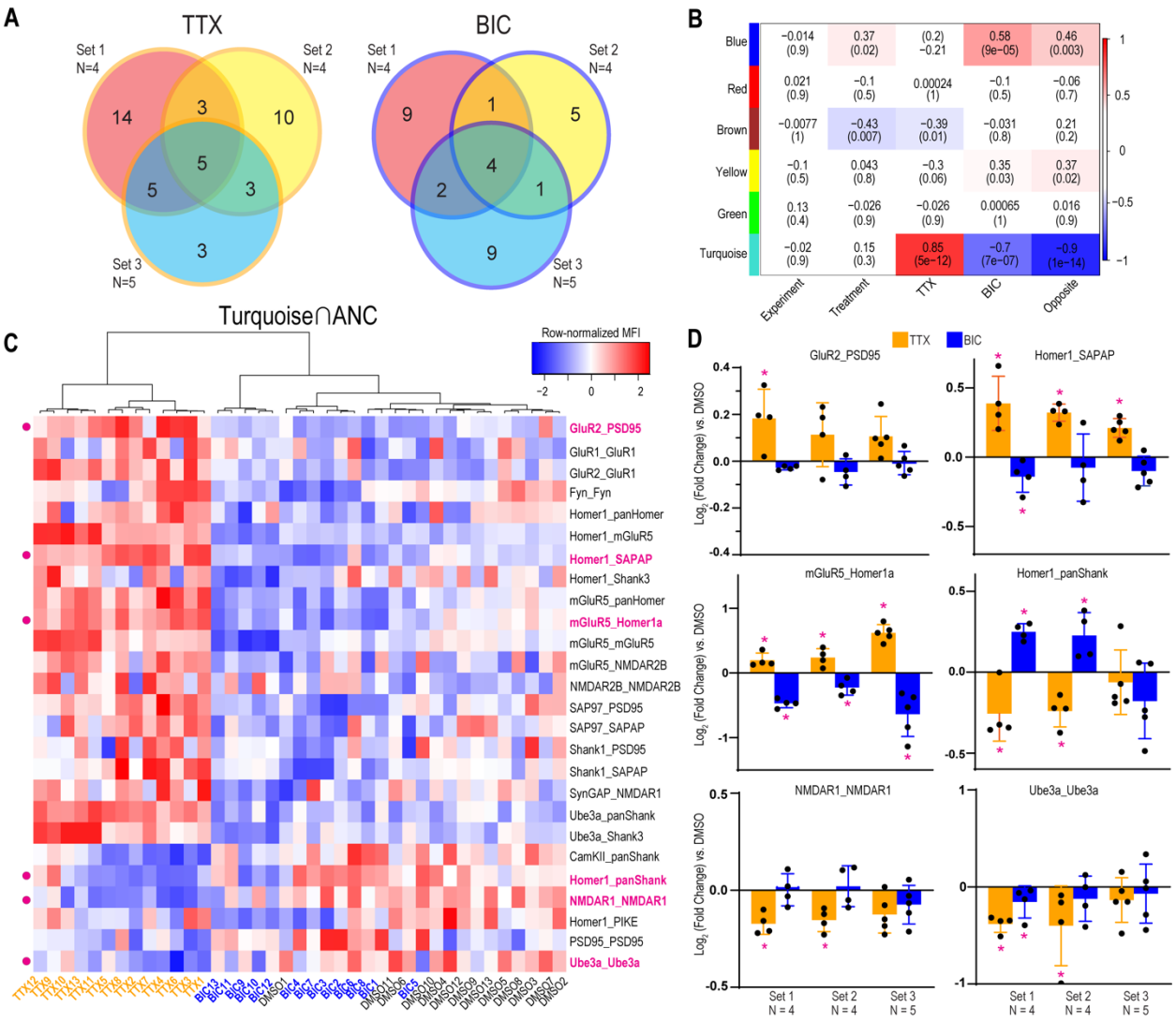

Figure 4

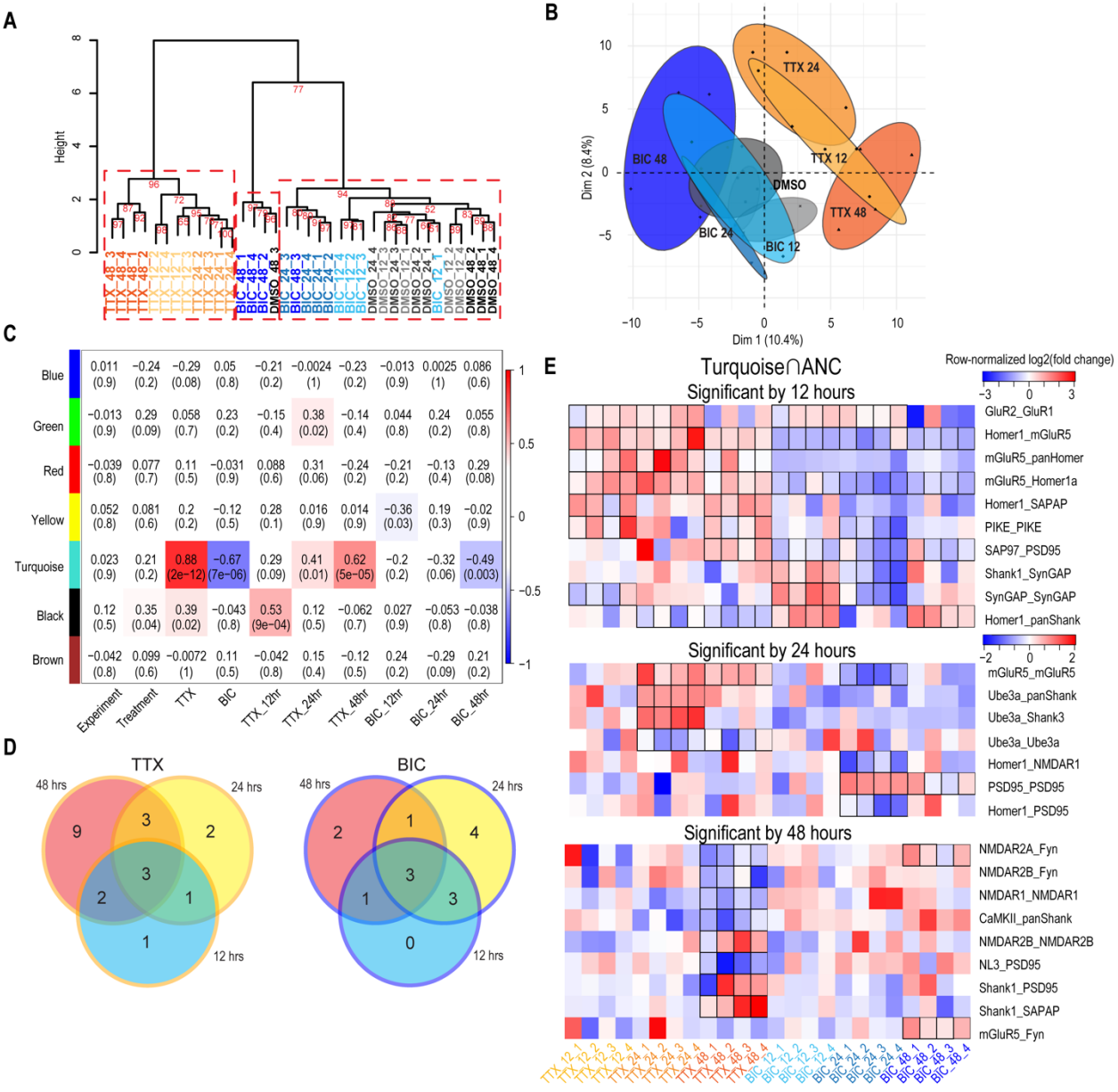

Figure 5

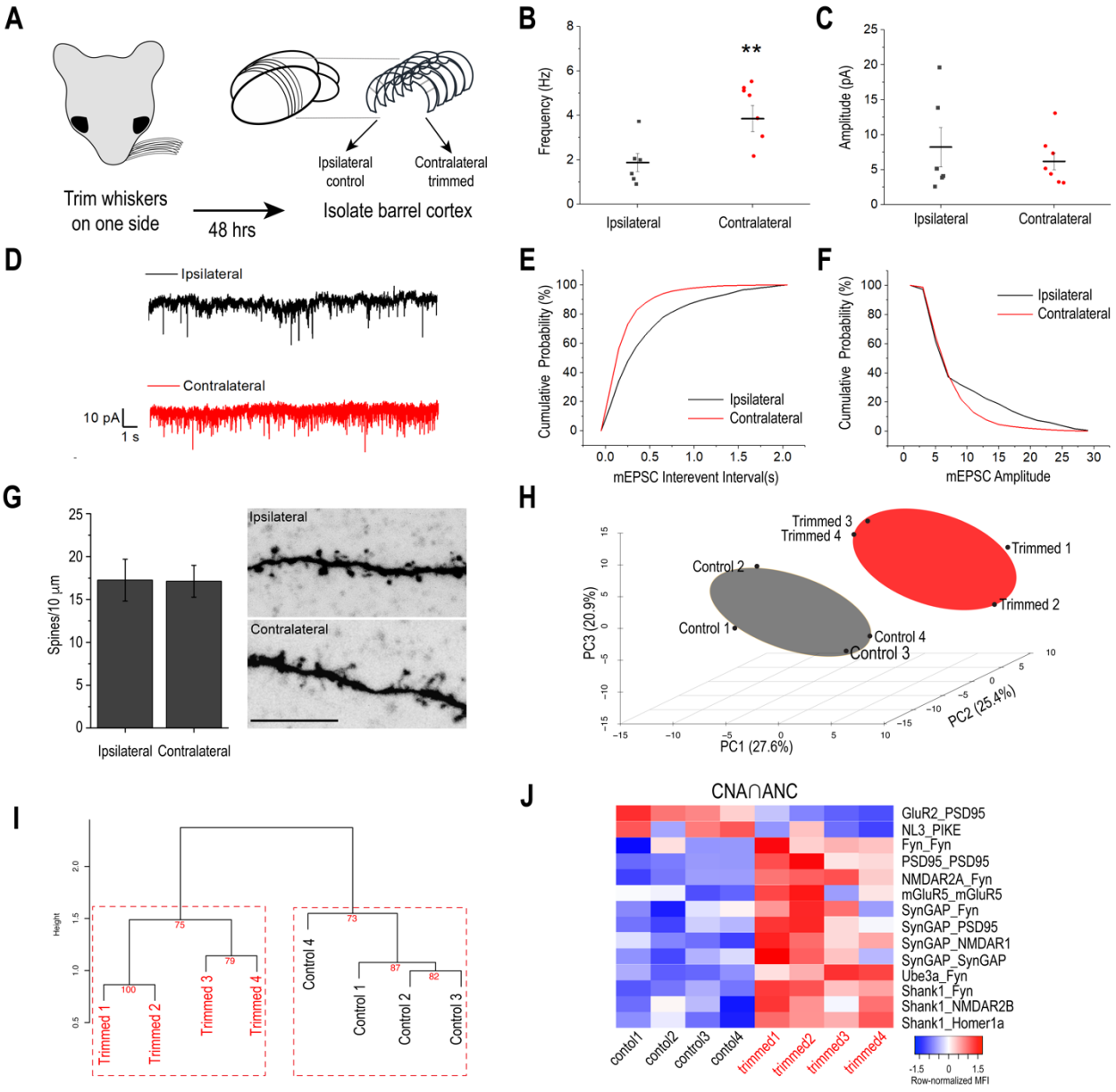

Figure 6

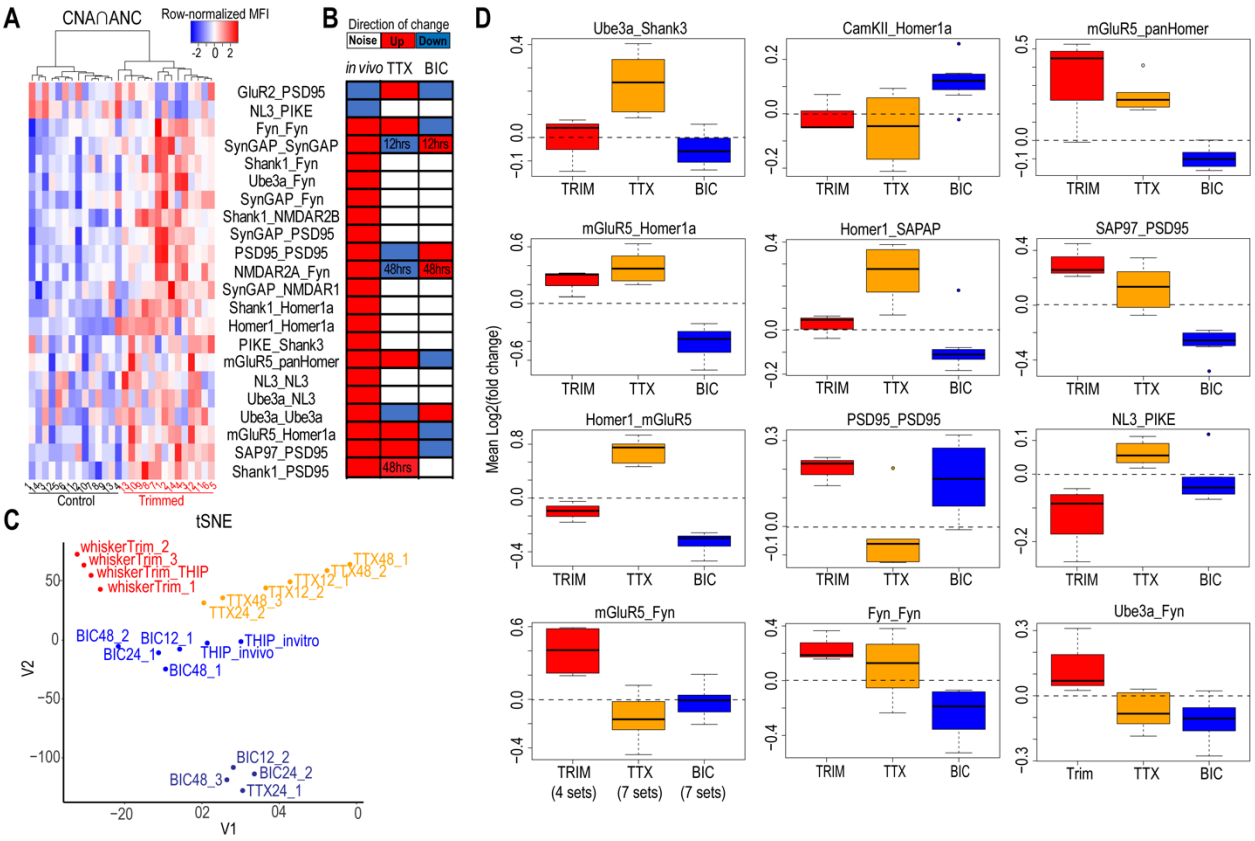

Figure 7

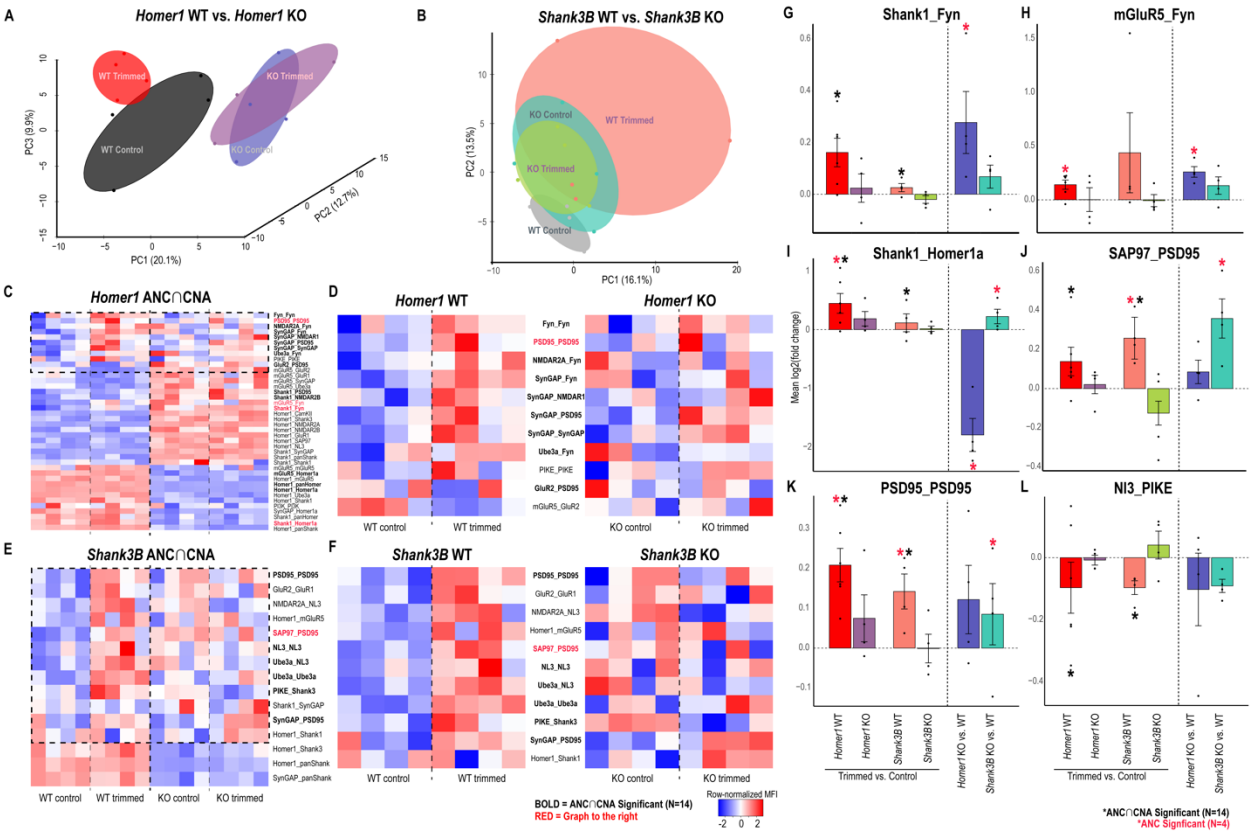

Table S1 Mean log2(fold change) of PiSCES that change significantly, as determined by ANC, after TTX or BIC treatment, and status in the bidirectional (turquoise) CNA module (N=4)

PiSCES	TTX mean log2(fold change)	BIC mean log2(fold change)	Turquoise Module(Y/N)
TTX-significant			
CamKII_panShank	-0.233875451		Y (MM<0.7)
Fyn_Fyn	0.128492332		Y
GluR1_GluR1	0.086777099		Y (MM<0.7)
GluR2_GluR1	0.355450115		Y
GluR2_PSD95	0.18305821		Y
Homer1_panHomer	0.126769282		Y
Homer1_mGluR5	0.802037751		Y
Homer1_Shank1	-0.14783399		N, Brown
mGluR5_Fyn	-0.456041901		N, Brown
mGluR5_mGluR5	0.178826159		Y
mGluR5_NMDAR2B	0.130164647		Y (P=0.07)
NMDAR1_NMDAR1	-0.171835916		Y
SAP97_SAPAP	0.12524575		Y
Shank1_Homer1a	-0.364753953		N
Shank1_panShank	-0.189669624		Y
SynGAP_Homer1a	-0.220079348		N
SynGAP_NMDAR1	0.211666705		Y
SynGAP_panShank	-0.195947874		N
Ube3a_panShank	0.103336032		Y (MM<0.7)
BIC-significant			
mGluR5_panHomer		-0.163969408	Y
PSD95_PSD95		0.253592446	Y
SAP97_PSD95		-0.184266356	Y
Shank1_NMDAR2B		0.178953408	N
Shank1_PSD95		-0.211392538	N, Brown
Shank1_Shank1		-0.477837091	N, Brown
SynGAP_Fyn		-0.190042269	N, Brown
SynGAP_PSD95		-0.318361093	N, Brown
Both-significant			
Ube3a_Ube3a	-0.380543347	-0.153786922	Y (MM<0.7)
Homer1_panShank	-0.256082657	0.249486122	Y
Homer1_SAPAP	0.38827265	-0.140848038	Y
mGluR5_Homer1a	0.199583157	-0.468645998	Y
NL3_SAPAP	-0.189515762	-0.229458554	N, Brown
Shank1_SAPAP	0.366638096	-0.304780053	Y
Shank1_SynGAP	-0.194247803	-0.214786859	N, Brown
SynGAP_SynGAP	-0.150728994	-0.202316192	N, Brown

Table S2. Top-ranked significantly different PiSCES between three models of homeostatic plasticity (Wilcoxon rank-sum test). PiSCES in bold are significantly different between the *in vivo* model and both *in vitro* models. N=7 sets (TTX), 7 sets (BIC), and 4 sets (Trim), 4 biological replicates per set.

TTX vs. BIC	*P*-value	TTX vs. Trim	*P*-value	BIC vs. Trim	*P*-value
CamKII_PIKE	0.003	CamKII_panShank	0.028	Fyn_Fyn	0.023
Homer1_mGluR5	0.003	GluR2_GluR1	0.028	**Homer1_mGluR5**	0.023
mGluR5_panHomer	0.003	**Homer1_mGluR5**	0.028	mGluR5_Homer1a	0.023
mGluR5_Homer1a	0.003	Homer1_SAPAP	0.028	SAP97_PSD95	0.023
SAP97_PSD95	0.003	**mGluR5_Fyn**	0.028	Ube3a_Fyn	0.023
Ube3a_panShank	0.003	NL3_PIKE	0.028	**mGluR5_Fyn**	0.040
Ube3a_Shank3	0.003	SynGAP_PSD95	0.028	mGluR5_panHomer	0.040
NMDAR1_NMDAR1	0.005	Ube3a_panShank	0.028	PIKE_PSD95	0.040
Homer1_SAPAP	0.008	Ube3a_Shank3	0.028	SynGAP_NMDAR1	0.040
NMDAR2B_SAPAP	0.008	**Ube3a_Ube3a**	0.028	**Ube3a_Ube3a**	0.040
Shank1_SAPAP	0.008				
Ube3a_Ube3a	0.008				
Homer1_NMDAR1	0.012				
mGluR5_mGluR5	0.012				
CamKII_Homer1a	0.018				
Homer1_panHomer	0.018				
PSD95_PSD95	0.018				
Fyn_Fyn	0.027				
Homer1_Shank1	0.027				
PIKE_PIKE	0.027				

Figure S1

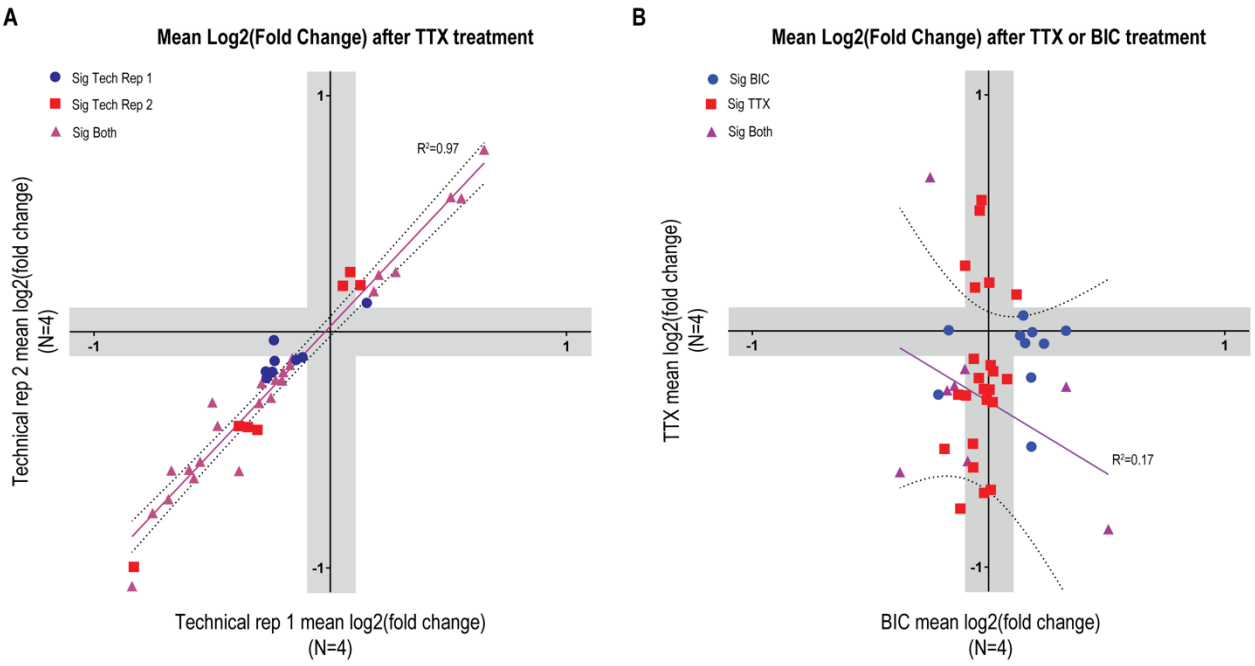

Figure S2

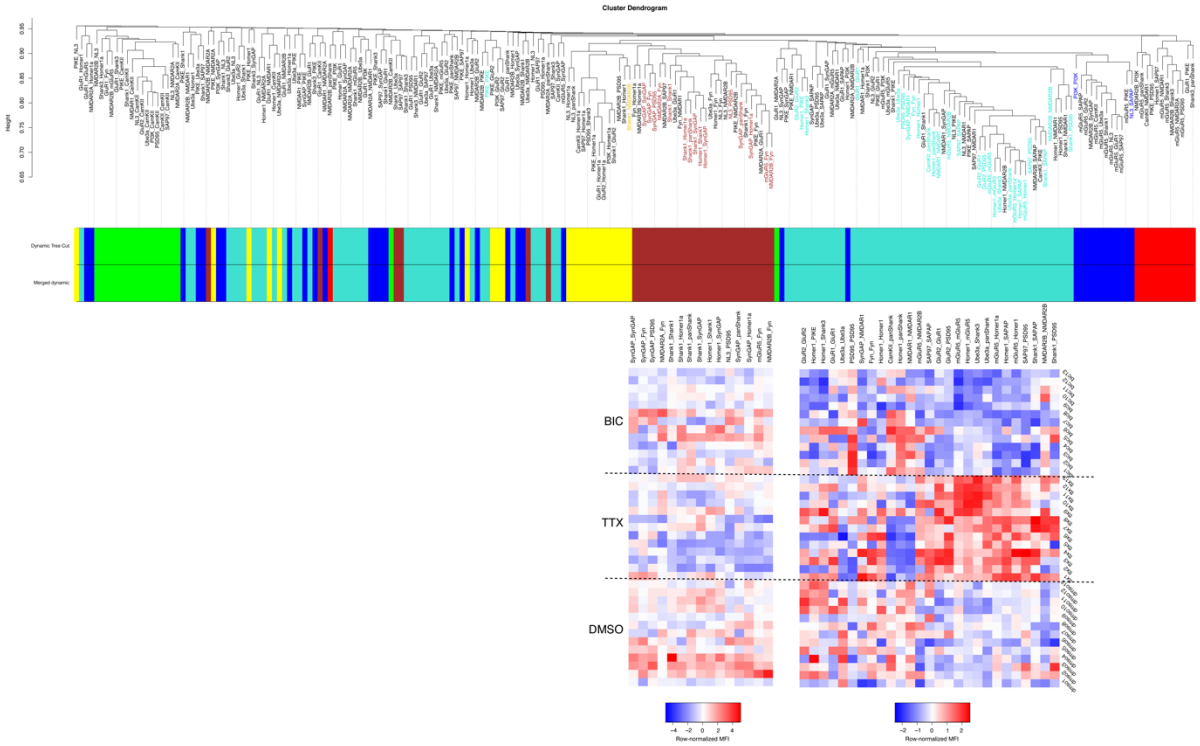

Figure S3

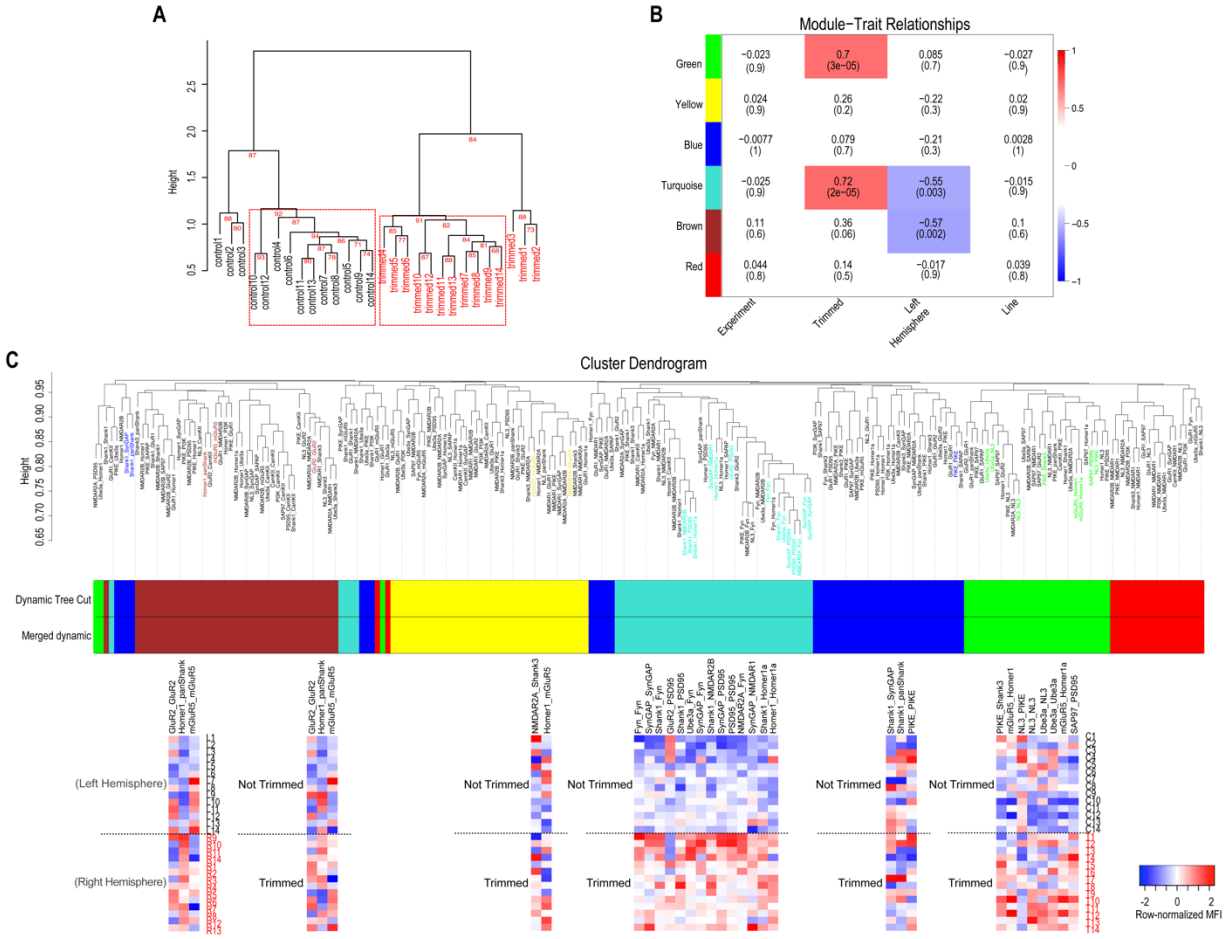

Figure S4